ACS Catalysis

pubs.acs.org/acscatalysis

Research Article

Assessing the Influence of Void Environment in MFI Zeolites on Propene Oligomerization Kinetics Using a Combined Computational and Experimental Approach

Lauren Kilburn, Diamarys Salomé Rivera, Elizabeth E. Bickel Rogers, Rajamani Gounder,* and David D. Hibbitts*

Cite This: *ACS Catal.* 2025, 15, 7121−7137

Read Online

ABSTRACT: The consequences of Brønsted acid site location in MFI zeolites were investigated for propene oligomerization. Adsorbates in MFI may reside in smaller channels (~5.5 Å diam.) or larger channel intersections (~7 Å diam.), with tighter confinement expected to enhance both stabilizing dispersive interactions and destabilizing steric constraints. MFI samples synthesized using tetrapropylammonium (TPA^+) as the structure directing agent have higher fractions of acid sites near intersections, while samples synthesized with 1,4-diazabicyclo[2.2.2]octane (DABCO) or ethylenediamine (EDA) have higher fractions of acid sites within channels. Measured propene dimerization rates (per H^+, 315 kPa C_3H_6, 503 K, 1.6 H^+/u.c.) are ~9 times higher on MFI-DABCO/MFI-EDA than MFI-TPA. Because propene oligomerization is transport-limited in MFI at these conditions, experimentally measured rates are proportional to both effective kinetic (k_{eff}) and diffusion (D_e) constants. DFT was therefore used to investigate the kinetic influences of void environment in isolation of transport effects. Adsorption free energies for C_3 and C_6 alkenes and dimerization free energy barriers were calculated at all 12 T-sites present in the MFI framework and all accessible O-sites around each T-site. C_3 preferentially adsorbs as H-bonded propene with similar energies in all void environments, while C_6 alkenes are destabilized by 10−56 kJ mol^{-1} and dimerization transition states are destabilized by 29−102 kJ mol^{-1}, on average, in the channels relative to intersections. The stability of C_3 and C_6 alkenes and dimerization transition states is largely governed by steric penalties arising from distortion of the MFI framework that outweigh stronger dispersive interactions with decreasing void size, even for species as small as C_3. Given that DFT predicts k_{eff} values are lower at acid sites in smaller channel voids of MFI, higher measured rates on MFI samples synthesized using DABCO or EDA must reflect less severe diffusion restrictions and, in turn, higher D_e values.

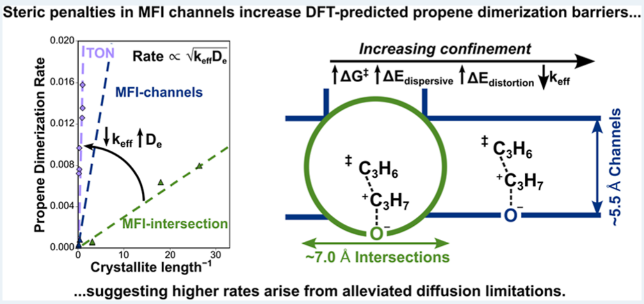

KEYWORDS: *zeolites, oligomerization, diffusion, confinement, void environment, sterics*

1. INTRODUCTION

Microporous aluminosilicate zeolites are commonly used as solid Brønsted acid catalysts,[1−3] with ~250 unique crystalline topologies that can be synthesized with distinct pore environments and interconnectivity.[4] Even within a given zeolite framework, multiple pore environments may exist; for example, the MFI framework consists of smaller ten-membered ring (10-MR) straight and sinusoidal channels (~5.5 Å diam.) and larger channel intersections (~7 Å diam.).[4,5] As such, extensive effort has been devoted to examining how the size and shape of the zeolitic pore impact reactive intermediates and transition states, and thus reaction rates, selectivities, and stabilities.[6−12] As the void size approaches that of the confined species, there is a trade-off between enthalpic stabilization via dispersive interactions and destabilization from the structural distortion of the zeolitic framework to accommodate adsorbates.[7,8,13,14] Confining voids may stabilize intermediates and transition states to varying extents when these moieties have different sizes and structures, leading to rates or selectivity that depend on void size.[7,10,13] Prior experimental work has typically studied confinement by varying the framework topology[13,15−17] or using post-synthetic methods to selectively titrate Brønsted acid sites in specific environments.[18,19]

Propene oligomerization is an interconnected series−parallel reaction network that includes β-scission and co-oligomerization pathways that produce a wide range of linear and branched alkene products (C_4−C_{12}) suitable as transportation

Received: January 17, 2025
Revised: March 18, 2025
Accepted: April 4, 2025

https://doi.org/10.1021/acscatal.5c00392

fuels,[20−22] and is one reaction for which confinement effects were previously studied by varying the zeolite framework topology.[13,23] Pseudo first-order rate constants for propene dimerization (per H^+, 503 K, <5% C_3H_6 conversion) increased with decreasing void size among TON (one-dimensional (1D), 5.7 Å diameter channels), MFI (3D, 5.5 Å diameter channels and 7.0 Å diameter intersections), BEA (3D, 6.9 Å diameter channels), FAU (3D, 11.9 Å diameter cages), and amorphous silica−alumina (ASA, >20 Å diameter pores).[13] Propene dimerization barriers and dispersive (van der Waals) interactions between adsorbates and the zeolite framework were estimated using DFT-D3 methods at one O-site in a TON channel (5.7 Å), an MFI intersection (7.0 Å), and a FAU cage (11.9 Å).[13] Dispersive interaction energies became increasingly exothermic as void size decreased, correlating with the increase in measured rate constants, leading to the interpretation that smaller void sizes preferentially stabilized the larger dimerization transition state (C_6H_{13}) over the smaller propyl−Z reactant (C_3H_7) through van der Waals interactions.[13] Subsequent work demonstrated the presence of strong transport limitations in medium pore, 10-MR zeolites arising from the occlusion of heavier molecular weight products formed during propene oligomerization, indicating that observed rate constants on medium-pore zeolites reflect a convolution of kinetic and transport effects at virtually all reaction conditions of interest.[24] A separate study comparing TON and MFI similarly reported higher propene dimerization rate constants on TON (per H^+, 10−600 kPa C_3H_6, 503 K) and suggested that these increases were caused by more effective stabilization of dimerization transition states and by the alleviation of transport restrictions caused by a shift in product selectivity to lighter molecular weight products ($\leq C_9$).[23] Although these prior data suggest that 10-MR channels stabilize dimerization transition states more effectively than larger 10-MR intersections or 12-MR channels, experimental rate measurements convolute transport and kinetic influences, motivating a theoretical study that can isolate kinetic behavior.

Transition state stability is influenced by confinement among different zeolite topologies and, by extension, confinement among different void environments within the same topology. Low-symmetry MFI zeolites have 12 crystallographically unique tetrahedral sites (T-sites) where Al atoms can reside, providing access to both channel and intersection environments. While MFI is typically synthesized with tetra-*n*-propylammonium (TPA^+) as the organic structure directing agent (OSDA), which biases the location of Brønsted acid sites near MFI intersections, recent work has shown that other OSDAs can alter acid site distributions.[25−27] MFI zeolites synthesized with nonconventional OSDAs—either 1,4-diazabicyclo [2.2.2] octane (DABCO) mixed with methylamine (1:1); or ethylenediamine (EDA) mixed with small amounts of TPA^+ (15:1)—demonstrated 4−9× lower toluene methylation rates (per H^+, 4 kPa toluene, 66 kPa dimethyl ether, 403 K) and higher selectivity to *para*-xylene (∼80%) compared to MFI samples synthesized with TPA^+ (∼30% *para*-xylene selectivity).[25] These toluene methylation data, unlike propene oligomerization, are measured at conditions of strict kinetic control and therefore uncorrupted by intrazeolite transport rates, as evidenced by invariant rates and selectivities across large changes in zeolite crystallite size (0.1−3.3 μm) within each family of MFI materials and invariant selectivities upon titration of external acid sites by 2,6-ditertbutylpyridine (DTBP). The kinetic differences observed between the TPA^+-based MFI samples and those derived from nonconventional OSDAs were attributed to shifts in acid site distribution with the assistance of DFT-predicted SDA−Al interaction energies and arene alkylation barriers. DFT-predicted barriers for toluene methylation transition states to form all three xylene isomers were higher in MFI channels compared to the larger intersections, consistent with lower overall rates, but *para*-xylene transition states were destabilized to a lesser extent in the channels compared to the larger *meta*-xylene and *ortho*-xylene isomers, consistent with higher *para*-xylene selectivity. DFT-predicted SDA−Al interaction energies, similarly, predicted more favorable Al-siting energies in channels using DABCO-methylamine[25] as the SDA complex as compared to using TPA^+,[26] which strongly favors Al siting at near-intersection T-sites. This study provides an example for how catalytic rate measurements can be combined with computational DFT to study the influence of void environment in MFI on kinetic rate constants, as we extend here to a coupled reaction-diffusion system.

Here, we measure propene dimerization rates on MFI samples (H^+/u.c. = ∼1.3) synthesized with TPA^+, DABCO, and EDA that are predicted to generate materials with acid sites primarily located in intersections (TPA^+-based) and or in channels (DABCO- and EDA-based). Propene dimerization rates (per H^+, 503 K) were ∼9× higher on MFI samples synthesized with EDA or DABCO compared to samples synthesized with TPA^+. Given that experimental measurements of propene oligomerization rates reflect coupled kinetic and transport influences, the kinetic influences of void environment were investigated independently using DFT. Adsorption energies of propene and all 13 hexene isomers were calculated with DFT at all accessible sites among the 48 T-O site-pairs in MFI. Transition states for propene dimerization, the first and likely rate-determining step in the oligomerization reaction network, were also studied at all accessible O-sites. Our results suggest C_3 most likely adsorbs as H-bonded propene, rather than as a bound alkyl (i.e., alkoxide), and that there is a weak influence of void environment on the stability of H-bonded propene. Hexene isomers are more stable in MFI intersections compared to channels and are more sensitive to void environment than propene as they are larger and more susceptible to steric penalties when confined in smaller void environments. Propene dimerization transition states are destabilized, relative to H-bonded propene precursors, in channels compared to the intersection, suggesting that the energetic penalty of framework distortions outweighs the stabilizing effects of enhanced dispersive interactions. These DFT data predict lower dimerization rate constants in smaller channel voids, suggesting that observed rate increases in DABCO- and EDA-based MFI over TPA^+-based samples reflect increases in effective propene diffusivities that exceed concomitant decreases in intrinsic rate constants.

2. METHODS

2.1. Experimental Methods. The MFI zeolite samples tested in this study were synthesized using different combinations of organic and inorganic SDAs according to previously reported protocols.[26,27] Furthermore, TON and MFI samples showed for comparison in this study were reported in previous publications.[23,28] Powder X-ray diffraction (XRD) and calculated micropore volumes from N_2 adsorption isotherms (77 K) were used to verify the framework topology

Table 1. Characterization Data of MFI Zeolites Synthesized With Different SDAs

sample[a]	SDAs[b]	Si/Al_{tot}[c](solid)	H^+/Al_{tot}[d]	H^+/u.c.[e]	Al^{IV}/Total NMR visible Al[f]	length[g]/μm
MFI-DABCO-3.3	DABCO, MA, Na^+	44	0.95	1.9	0.98	3.3 ± 0.6
MFI-DABCO-12.7	DABCO, MA, Na^+	44	0.85	1.8	0.98	12.7 ± 2.1
MFI-EDA-8.2	EDA, TPA^+	58	0.92	1.6	0.97	8.2 ± 1.6
MFI-C_{666}-0.03	C_{666}, Na^+	47	0.81	1.3	0.97	0.03 ± 0.01
MFI-TPA-0.06	TPA^+,Na^+	54	0.80	1.4		0.06 ± 0.01
MFI-TPA-0.33	TPA^+,Na^+	55	0.84	1.4		0.33 ± 0.07

[a]Sample nomenclature is MFI-X-Y, where X indicates the major organic OSDA, and Y denotes the crystallite size measure by SEM. [b]SDAs used during synthesis. [c]Determined by ICP-OES. Uncertainty is ±10%. [d]Determined from liquid-phase NH_4 ion exchange followed by NH_3 TPD. Uncertainty is ±10%. [e]Calculated from elemental analysis and unit cell formula. [f]Calculated from ^{27}Al solid-state NMR. Al^{IV} corresponds to the 56 ppm signal and spinning side bands and uncertainty is ±0.05. [g]Average crystallite size estimated by SEM. Uncertainties are represented by standard deviation.

and crystallinity of MFI and TON samples. The number of proton sites initially present on each sample prior to reaction (H_0^+) was quantified by NH_3 temperature-programmed desorption (NH_3 TPD). NH_3 TPD experiments were not used to assess acid strength to avoid the previously documented difficulties with interpreting NH_3 TPD profiles,[29−31] but the individual profiles are reported in Section S2.3 of the Supporting Information. Elemental analysis was performed to quantify the corresponding amounts of Si and Al present in each sample. Detailed synthesis procedures and characterization techniques are discussed in Section S1 and S2 of the Supporting Information. Propene oligomerization reactions were performed in a stainless-steel tubular reactor where the effluent composition was analyzed using a gas chromatograph (GC). Dimerization rates were estimated from rates of product formation using eq 1:

$$r_{\text{dim}} = r_6 + r_9 + \frac{1}{2}(r_4 + r_5 + r_7 + r_8 + r_{10}) \tag{1}$$

where r_n corresponds to the rate of formation of products of carbon number n to consider the formation of products different than dimers (detailed discussion of eq 1 can be found in previous reports[24,28]). We do not report a carbon balance as the difference in propene peak areas quantified by the GC before and during the reaction is within experimental error at the low conversions we studied ($X \leq 1\%$).

Absolute errors in measured rates were calculated by propagating the uncertainties relating the quantification of the number of H_0^+ sites, the amount of catalyst loaded, and the errors from fluctuations in the reactant GC peak areas compared to the internal standard when bypassing the reactor. Moreover, steady-state rate was reported as the value measured after dimerization rates changed <4% over 8 ks to account for samples that continued to decrease slightly over time. More information about the reactor setup and data analysis is provided in Section S3 of the Supporting Information.

2.2. Computational Methods.

DFT calculations were performed using the Vienna ab initio simulation package (VASP)[32−35] executed in the computational catalysis interface (CCI).[36] Projector augmented wave (PAW) potentials were used to build planewaves with an energy cutoff of 400 eV.[37] The Perdew−Burke−Ernzerhof (PBE) exchange correlation functional[38] was used with the DFT-D3 method with Becke−Johnson (D3BJ) damping to capture dispersive interactions.[39,40]

DFT calculations were performed using the MFI unit cell obtained from van Koningsveld[41] with fixed unit cell parameters (a = 20.090 Å, b = 19.738 Å, c = 14.7670 Å, $\alpha = \beta = \gamma = 90°$) because this zeolite structure is less susceptible to restructuring during optimization.[42] MFI has 12 crystallographically unique T-sites each bound to 4 O-sites, generating 48 T/O site-pairs. C_3-derived adsorbates (1-propyl−Z, 2-propyl−Z, and H-bonded propene), C_6 H-bonded alkenes (*n*-hexene, 2-methylpentene, 3-methylpentene, 2,3-dimethylbutene, and 3,3-dimethylbutene) and dimerization transition states were examined at all accessible O-sites. T-sites and O-sites were labeled according to the indices from the International Zeolite Association (IZA).[4] This index, along with the corresponding labeling from van Koningsveld,[41] is listed in Table S2 of the Supporting Information. Gas phase calculations of propene and C_6 alkene isomers were modeled in a 15 × 15 × 15 Å^3 vacuum unit cell. No atoms were constrained (frozen) during structural optimizations, pathway calculations, or transition state searches.

Structures were optimized in a two-step process using a fast Fourier transform (FFT) grid to calculate forces. Structures were first converged to $<10^{-4}$ eV energy variation between iterations and a max force of <0.05 eV Å^{-1} per atom with an FFT cutoff 1.5× the planewave cutoff. They were subsequently converged with an energy variation of $<10^{-6}$ eV between iterations and the same max force of <0.05 eV Å^{-1} with a cutoff 2× the planewave cutoff. This method was chosen because it is ∼3× more efficient than a single-step optimization.[36] The Brillouin zone was sampled at the gamma point.[43]

Propene dimerization was modeled at O25 of T11 using the nudged elastic band (NEB) method[44] with 16 images and converged until forces on all atoms were <0.5 eV Å^{-1} per atom. The dimerization transition state was then isolated using the Dimer method[45] and optimized using the two-step method described above until the force per atom was <0.05 eV Å^{-1}. The O25 dimerization transition state structure was then relocated and reoptimized at the remaining 47 O-sites using the two-step optimization method.

All optimized adsorbate and transition state structures were systematically reoriented according to the method detailed in our prior study[46] to increase the probability of finding the global energy minima and most energetically favorable transition states. Reorientations were performed based on the interactions of each state with the framework. Although this method does not guarantee the global minima will be obtained, it was shown to decrease DFT energies from user-generated structures by 10−50 kJ mol^{-1} while being ∼100× less computationally expensive than ab initio molecular dynamics and is readily accessible to rigorous transition state searches absent any constraints.

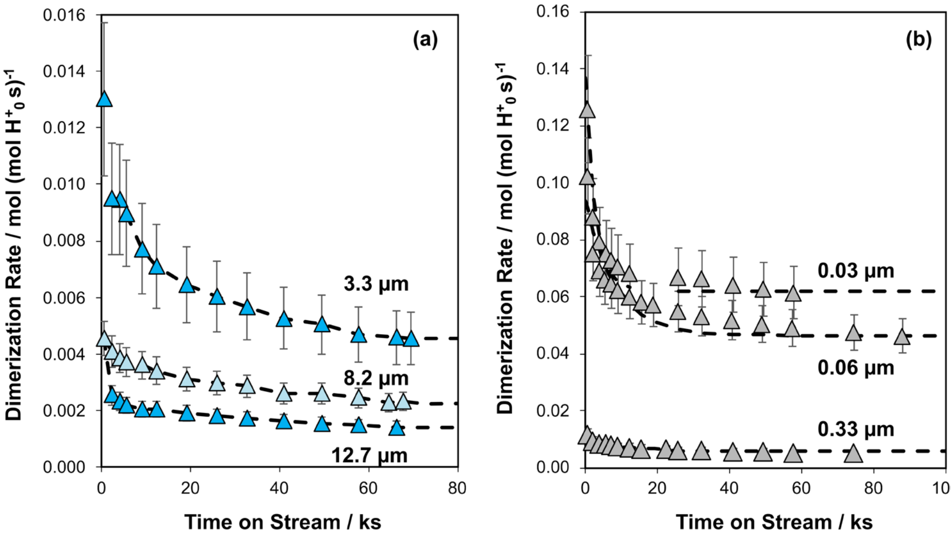

Figure 1. Dimerization rates measured at 503 K, 315 kPa C_3H_6 plotted against time on stream for (a) MFI-DABCO (dark blue) and MFI-EDA (light blue) series used in this study and for (b) MFI-TPA series with different crystal sizes adapted from Bickel et al.[28] Copyright 2023 American Chemical Society. Error bars reflect absolute values.

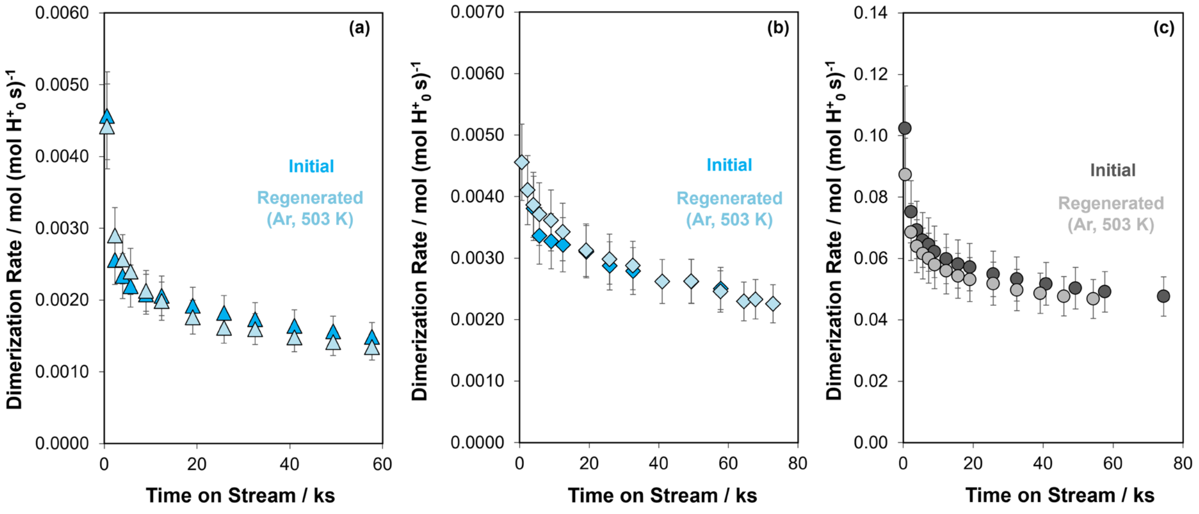

Figure 2. Measured dimerization rates (503 K, 315 kPa) initially (dark blue or dark gray) and after regeneration in flowing Ar (50 ks, light blue or light gray) on (a) MFI-DABCO-12.7 (triangles) and (b) MFI-EDA-8.2 (diamonds) used in this study and (c) MFI-TPA-0.06 (circles) adapted from Bickel et al.[28] Copyright 2023 American Chemical Society. Error bars reflect absolute values.

Vibrational frequencies were calculated for the lowest energy structures of all states using a fixed displacement method, wherein all adsorbate atoms and the T-site (AlO_4^-) were displaced. Vibrational frequencies were then used to calculate zero-point vibrational energies (ZPVE) and temperature-corrected enthalpies (H), entropies (S) and free energies (G) according to the equations in Section S6 of the Supporting Information. Except for imaginary modes along the reaction coordinate, low frequency vibrational modes (<60 cm^{-1}) were replaced with 60 cm^{-1} to improve the accuracy of entropy estimations, as done in previous studies.[47−49]

3. RESULTS AND DISCUSSION

3.1. Experimental Results. A summary of the physicochemical properties of MFI zeolites synthesized with different SDAs and varied crystal sizes (0.06−3.3 μm) is shown in Table 1. MFI samples have similar H^+ content (Si/Al ~ 50, H^+/u.c. ~ 1.6) and the majority of Al incorporated in the framework as quantified by NH_3 TPD (H_0^+/Al_{tot} > 0.80) and ^{27}Al solid-state NMR (Al^{IV}/Total NMR visible $Al^f \geq 0.97$) from,[25] but were synthesized with different combinations of organic and inorganic SDAs (synthesis details and characterization data, Sections S1 and S2, Supporting Information). MFI-DABCO samples were synthesized using a 1:1 mixture of DABCO and methylamine, while MFI-EDA was prepared with EDA and minor quantities of TPA^+ as the co-OSDA (EDA/TPA^+ = 15). Additionally, MFI-TPA samples (previously reported in studies of propene oligomerization reactions[24,28]) prepared using the conventional OSDA (TPA^+) and a TPA^+-like diquaternary ammonium OSDA (C_{666}) are shown in Table 1. While NMR spectra were not measured directly on all samples, our previous work examining toluene methylation kinetics showed that Al^{IV}/Al_{tot} values did not vary systematically between the TPA-based materials (0.96−0.98) and the materials synthesized using EDA (0.97−0.99) or DABCO (0.98).[25] Based on this previous work using these same

Scheme 1. Reaction Scheme for Propene Dimerization on the Zeolite Acid Site (H−Z)

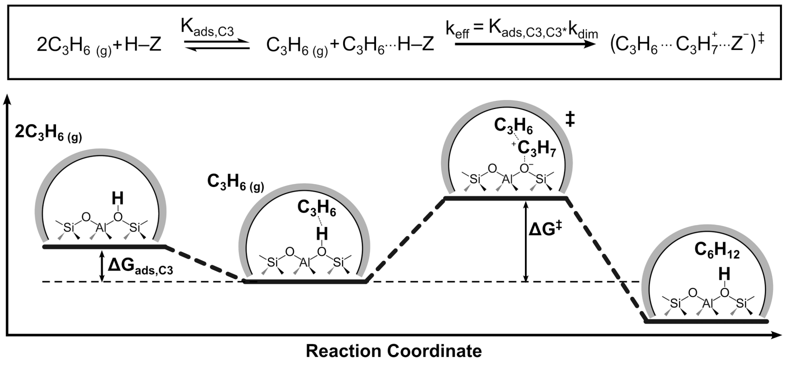

materials,[25] we conclude these MFI samples contain similar H^+ site density (H^+/u.c. ∼1.7) and varied crystal sizes (0.03−12.7 μm), wherein MFI-TPA samples contain predominantly H^+ sites in larger channel intersections while MFI-DABCO/MFI-EDA samples contain significant fraction of H^+ sites in smaller channel environments. Our MFI-TPA samples (0.06−0.33 μm) are expected to behave similarly to commercial MFI samples with comparable crystal size based on our prior comparisons between commercially sourced samples and TPA-synthesized materials.[13,25,28,50]

Propene dimerization rates (per H_0^+, 503 K, 16−605 kPa C_3H_6, conversion ≤1%) were measured on MFI-DABCO and MFI-EDA samples of varied crystallite size (3.3−12.7 μm). Dimerization rates decreased with time-on-stream and approached steady-state values for all samples at 315 kPa C_3H_6 (Figure 1a) and at other propene pressures (16 and 615 kPa C_3H_6, Figure S16, Supporting Information). After purging in Ar at reaction temperature (503 K), initial rates and subsequent transient decrease with time-on-stream were recovered (Figure 2). Regeneration of the catalyst in an inert gas, in contrast to a high temperature (>793 K) oxidative treatment, indicates deactivation caused by the accumulation of highly saturated products (e.g., alkenes) and not the blocking of acid sites by highly unsaturated polyaromatic coke precursors. Regeneration in an inert or vacuum treatment (673 K) following alkene oligomerization was similarly observed in prior studies on MFI,[51,52] as well as in our own work,[24,28] and attributed to the removal of an occluded hydrocarbon phase.

These occluded products inhibit the diffusion of propene and alkene products by decreasing their effective diffusivities, thereby imposing diffusional constraints on measured rates.[24] Transport limitations are evident from steady-state dimerization rates (per H_0^+, 503 K) that systematically decrease with increasing crystallite size within either the MFI-DABCO or MFI-EDA series of samples (Figure 1a), and as reported previously for MFI-TPA series of samples (Figure 1b),[28] as expected when measured rates are limited by intrazeolite diffusion. Furthermore, the extent of the imposed transport limitations is dependent on the composition of the intrapore alkene phase, which was shown to be sensitive to reaction conditions (temperature and pressure) and zeolite properties (acid site density and framework topology).[23,24,28]

The derivation of an effective rate constant (k_{eff}) for propene dimerization, measured coupled with diffusion, was discussed in previous literature and will be summarized here.[24] DFT-calculated barriers are higher for C−C coupling compared to product desorption,[13,53] and isotopic scrambling experiments demonstrating facile double bond isomerization are consistent with C−C bond formation as the rate-determining step.[54] C_3H_6 first adsorbs at a bare H−Z site (K_{ads,C_3}):

$$\mathrm{HZ} + C_3H_6(g) \rightleftharpoons (C_3H_6) - \mathrm{HZ} \qquad K_{ads,C3} \tag{2}$$

followed by a second adsorption of gas-phase C_3H_6 near a C_3H_6−Z species (K_{ads,C_3,C_3*})

$$C_3H_6 - \mathrm{HZ} + C_3H_6(g) \rightleftharpoons (C_3H_6)_2 - \mathrm{HZ} \qquad K_{ads,C3,C3*} \tag{3}$$

and the subsequent dimerization of the two C_3H_6 molecules (k_{dim})

$$(C_3H_6)_2 - \mathrm{HZ} \rightarrow C_6H_{12} - \mathrm{HZ} \qquad k_{dim} \tag{4}$$

as outlined in Scheme 1. The absence of IR features associated with OH stretching in MFI (10 kPa C_3H_6) suggests the surface is covered,[13] and measured first-order rates are consistent with a surface covered in a C_3H_6-derived species, likely a H-bonded propene or a propyl species bound to the zeolite framework O atom. We can then write the following rate equation for C_3H_6 dimerization on a C_3H_6-covered surface

$$\frac{r_{dim}}{L} = \frac{K_{ads,C3}K_{ads,C3,C3*}k_{dim}[C_3H_6]^2}{K_{ads,C3}[C_3H_6]} = K_{ads,C3,C3*}k_{dim}[C_3H_6] = k_{eff}[C_3H_6] \tag{5}$$

where K_i and k_i terms are defined for eqs 2−4 above, $[C_3H_6]$ is the pressure of propene (normalized by 1 bar standard pressure), and k_{eff} ($=K_{ads,C_3,C_3*}k_{dim}$) is the effective first-order rate constant for the reaction under kinetically controlled conditions. This effective rate constant can be written in terms of the difference in free energy of the transition state relative to the first adsorbed C_3H_6 species ($\Delta G^{\ddagger}$)

$$k_{eff} = \frac{k_B T}{h} e^{-\Delta G\ddagger/RT} \tag{6}$$

As described above, propene oligomerization rates at steady-state are influenced by intrazeolite diffusion restrictions caused by transport barriers introduced by accumulation of large alkene products within the zeolite pores. Therefore, effectiveness factor formalisms were used to examine the dependence of measured dimerization rates on crystallite size. In the limit of strong mass transport limitations, the effectiveness factor becomes the inverse of the Thiele modulus (Φ), irrespective of catalyst geometry, such that the observed rate can be written as a function of a characteristic path length, L:[28]

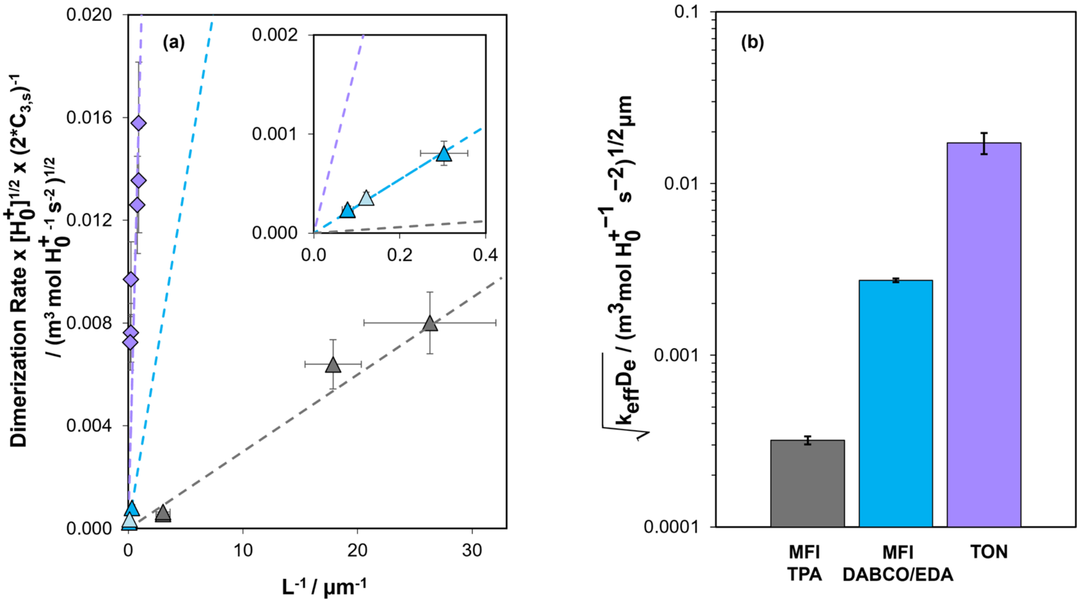

Figure 3. (a) Steady-state propene dimerization rates, normalized according to eq 8, as a function of the inverse of crystallite size for TON (purple diamonds) from ref 23, MFI-TPA (gray triangles) from ref 28, MFI-DABCO (dark blue triangles), and MFI-EDA samples (light blue triangles). Inset graph depicts the lower limits of the figure axes. Dashed lines represent linear regressions to eq 8. (b) Steady-state $\sqrt{k_{\mathrm{eff}}D_{\mathrm{e}}}$ values for propene dimerization (503 K, 315 kPa C_3H_6) for MFI-TPA, MFI-DABCO/EDA and TON. Error bars reflect the error in the data regressed to eq 8.

$$r_{\mathrm{dim,obs}} = \sqrt{\frac{k_{\mathrm{eff}}D_{\mathrm{e}}}{[\mathrm{H}_0^+]}}\left(\frac{2}{L}\right)C_{3,\mathrm{s}} \tag{7}$$

where $[\mathrm{H}_0^+]$ is the number of active sites per crystallite volume, L is the characteristic path length for diffusion (taken here as the average length of the shortest dimension of the crystallite), and D_{e} is the effective intrazeolite diffusivity of propene within the zeolite micropore. Rearrangement of eq 7 gives a linear expression

$$\frac{r_{\mathrm{dim,obs}}[\mathrm{H}_0^+]^{1/2}}{2C_{3,\mathrm{s}}} = \sqrt{k_{\mathrm{eff}}\mathrm{D}_{\mathrm{e}}}\left(\frac{1}{L}\right) \tag{8}$$

such that normalized rates are linearly proportional to L^{-1}, with a slope that reflects a convolution of kinetic and transport effects: $\sqrt{k_{\mathrm{eff}}D_{\mathrm{e}}}$. Measured rates on MFI-DABCO and MFI-EDA samples, and for MFI-TPA and TON samples reported in previous work,[23,28] indeed depend on L^{-1} as shown for 315 kPa C_3H_6 in Figure 3 (and at 16 and 605 kPa, Figure S16 of Supporting Information).

Values of $\sqrt{k_{\mathrm{eff}}D_{\mathrm{e}}}$ on MFI samples synthesized with TPA were ~9× lower than MFI samples synthesized using either EDA or DABCO and were ~54× lower than on TON (Figure 3b). MFI channels are similar in diameter (~5.5 Å diameter) to the unidirectional straight channels of TON (~5.7 Å diam), and MFI-EDA and MFI-DABCO materials were shown to have similar *p*-xylene selectivities to TON materials in our prior study of toluene methylation kinetics.[25] Taken altogether, $\sqrt{k_{\mathrm{eff}}D_{\mathrm{e}}}$ values increase as the size of confining voids around H^+ sites decrease (Table 2), and this is also observed at lower (16 kPa) and higher (605 kPa) propene pressures (Table 2), suggesting that MFI-EDA and MFI-DABCO materials consistently have higher $\sqrt{k_{\mathrm{eff}}D_{\mathrm{e}}}$ values than MFI-TPA zeolites. Variations in $\sqrt{k_{\mathrm{eff}}D_{\mathrm{e}}}$ values across pressures arise because propene pressure influences product distributions and therefore the nature of the occluded alkenes that fill MFI pores, and thus would influence D_{e} values.

Table 2. Steady-State $\sqrt{k_{\mathrm{eff}}D_{\mathrm{e}}}$ Values for Propene Dimerization (503 K) at Different C_3H_6 Pressures

sample	$\sqrt{k_{\mathrm{eff}}D_{\mathrm{e}}}$ /(m^3 mol H_0^{+-1} s^{-2})$^{1/2}$ μm		
	16 kPa C_3H_6	315 kPa C_3H_6	605 kPa C_3H_6
MFI-TPA	2.13×10^{-3}	3.20×10^{-4}	1.82×10^{-4}
MFI-DABCO/EDA	5.05×10^{-2}	2.73×10^{-3}	2.08×10^{-3}
TON	8.57×10^{-2}	1.73×10^{-2}	1.41×10^{-2}

This increase in $\sqrt{k_{\mathrm{eff}}D_{\mathrm{e}}}$ values with decreasing void size is consistent with prior work, where rate constants followed a trend based on void size as TON > MFI > BEA > FAU > ASA.[13] This was rationalized by stronger van der Waals interactions in smaller void environments that preferentially stabilized the dimerization transition state relative to the propene-derived precursor.[13] However, these measured propene dimerization rates, as evident in their dependence on crystallite size in Figure 3a, reflect a convolution of kinetic and transport properties. To distinguish between these influences, we next turn to DFT to assess the kinetic influences of acid site location in MFI on propene dimerization reactions to gain insights into the changes in $\sqrt{k_{\mathrm{eff}}D_{\mathrm{e}}}$ measured between MFI-EDA/MFI-DABCO and MFI-TPA samples.

3.2. Adsorption Energies of Propene.

As shown in Scheme 1, k_{eff} values depend on the stability of a bound propene, as well as the stability of the dimerization transition state, such that an effective free energy barrier ($\Delta G^{\ddagger}$) can be described as the energy difference between these two states

$$\Delta G^{\ddagger} = G_{[\mathrm{C_6H_{13}^+}-\mathrm{Z}^-]^{\ddagger}} - G_{\mathrm{C_3H_6^*}} - G_{\mathrm{C_3H_6(g)}} \tag{9}$$

Therefore, we start by considering how acid site location influences propene adsorption energies.

Upon propene adsorption at a Brønsted acid site, its C═C double bond can interact with the proton to form a H-bonded propene (Figure 4a), or a C atom can react with the proton to form a chemisorbed primary 1-propyl−Z (Figure 4b) or secondary 2-propyl−Z (Figure 4c) bound to a lattice oxygen. We evaluated how the void environment influences the individual and relative stabilities of all three species by calculating adsorption Gibbs free energies ($\Delta G_{\text{ads,C}_3}$, kJ mol^{-1}):

$$\Delta G_{\text{ads,C}_3} = G_{\text{C}_3{}^*} - (G_{\text{H-Z}} + G_{\text{C}_3\text{H}_6\text{(g)}}) \qquad (10)$$

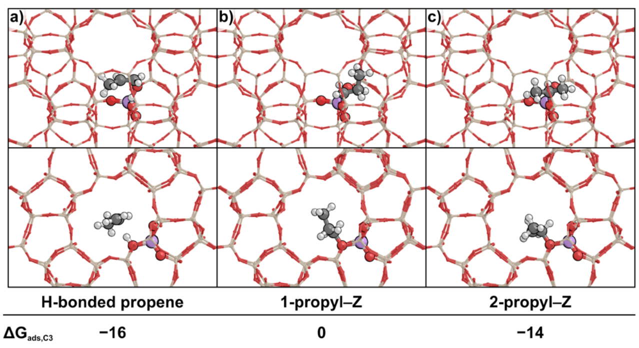

Figure 4. Adsorption free energies ($\Delta G_{\text{ads,C}_3}$ kJ mol^{-1}, eq 10) at 503 K for propene adsorbed as (a) H-bonded propene, (b) 1-propyl−Z, and (c) 2-propyl−Z at MFI O25/T12 viewed through the sinusoidal (top) and straight (bottom) channels.

for 1-propyl−Z, 2-propyl−Z, and H-bonded propene at all accessible O-sites in MFI (Figure 5a). Of the 48 T/O-sites, 6 (those at O4, O20, and O24) are inaccessible to propene as they are in 4-MR and 5-MR subunits of MFI. DFT calculations suggest H-bonded propene is the most stable adsorbate at 40 out of the 42 remaining O-sites, and 2-propyl−Z is the most stable at the remaining 2 O-sites (Figure 5). Prior oligomerization literature suggested 2-propyl−Z as the most likely C_3 intermediate, based on binding free energies (503 K) at O3/T2 on TON from DFT[55] and binding enthalpies (513 K) at T12 in MFI from ab initio QM/MM calculations[53] indicating 2-propyl−Z was ∼10 kJ mol^{-1} more stable than H-bonded propene. Computational studies comparing the stability of H-bonded alkenes, alkeniums, and alkoxides using DFT with an MP2 correction predicted more favorable adsorption free energies for H-bonded alkenes compared to alkoxides for C3−C5 species in FER (323 and 623 K)[56] and C_4−C_9 species in CHA (673 K).[57] Our static DFT calculations predict H-bonded propene as the more favorable binding mode compared to prior DFT work likely because our adsorbate-specific reorientations found more stable structures by considering numerous configurations, demonstrating that the accuracy of DFT can be improved through this reorientation method. Although much work has been devoted to elucidating the binding mode of these adsorbates, experiments indicate alkene protonation and deprotonation is rapid compared to C−C bond formation and cleavage over a wide temperature range (473−856 K); thus, interconversion between surface-bound alkyls and H-bonded alkenes should be facile.[54,58−60] It is therefore reasonable to assume that C_3 adsorbates are quasi-equilibrated, can interconvert between alkyl and H-bonded alkenes, and can easily alternate between the accessible O-sites at each T-site.

O-sites were categorized based on the void environment within which they reside (Table S2, Supporting Information), but it is important to note that although framework O atoms can be assigned to a specific environment, it does not prevent an adsorbate from accessing a different environment nearby. On average, $\Delta G_{\text{ads,C}_3}$ values (for all three forms of C_3) are lower in intersections compared to the straight or sinusoidal channel environments. Comparing intersections to channels, $\Delta G_{\text{ads,C}_3}$ values of H-bonded propene are 9 kJ mol^{-1} lower (indicating more favorable adsorption) in intersections than in either channel, indicating a weak preference for intersection environments. $\Delta G_{\text{ads,C}_3}$ values of 2-propyl−Z and 1-propyl−Z, in contrast, are ∼20−40 kJ mol^{-1} less stable in channels than

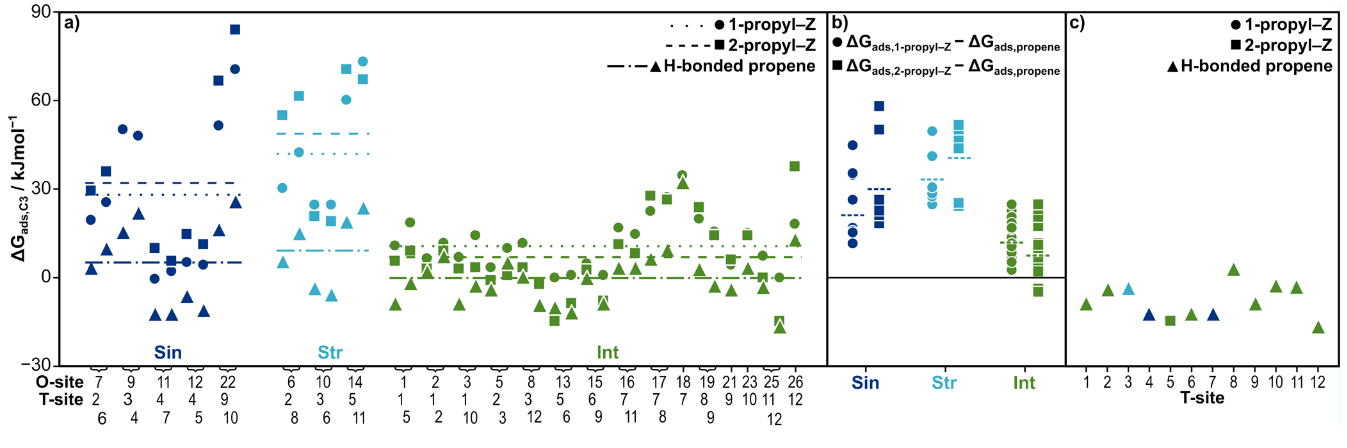

Figure 5. (a) Adsorption free energies ($\Delta G_{\text{ads,C}_3}$ kJ mol^{-1}, eq 10) for 1-propyl−Z (circles), 2-propyl−Z (squares), and H-bonded propene (triangles) in the sinusoidal channel (dark blue), straight channel (light blue), and intersection (green) at 503 K. Average $\Delta G_{\text{ads,C}_3}$ per C_3 adsorbate in each environment are denoted with lines (dotted for 1-propyl−Z, dashed for 2-propyl−Z, and long dashes for H-bonded propene). (b) The difference between the adsorption free energy of 1-propyl−Z and H-bonded propene ($\Delta G_{\text{ads,1-propyl-Z}} - \Delta G_{\text{ads,H-bonded propene}}$) and between 2-propyl−Z and H-bonded propene ($\Delta G_{\text{ads,2-propyl-Z}} - \Delta G_{\text{ads,H-bonded propene}}$) at all T/O-sites. (c) The lowest $\Delta G_{\text{ads,C}_3}$ of all C_3 adsorbates per T-site. A reorganized version of this figure organized by T-site instead of O-site (Figure S19) and structural images of the best C_3 adsorbate per T-site (Figures S22 and S33) are included in the Supporting Information.

in the intersections, indicating a greater extent of destabilization for both alkyls relative to H-bonded propene in the more confined channels. This is alternatively evinced by plotting the differences in adsorption energies between the propyl and H-bonded propene forms (Figure 5b). In sinusoidal and straight channels, the propyl−Z forms are ∼20 to ∼40 kJ $\mathrm{mol^{-1}}$ less stable than their H-bonded propene counterparts, and 1-propyl−Z is more stable than 2-propyl, which is more sterically hindered. In intersections, the propyls are only slightly less stable (5−10 kJ $\mathrm{mol^{-1}}$ shifts in average $\Delta G_{\mathrm{ads,C_3}}$ values) than their propene counterparts, and 2-propyl−Z is more stable on average than 1-propyl, as expected for an unconfined site because the secondary C in 2-propyl−Z is more suited to handle its partial positive charge.

Given that C_3 adsorbates are expected to be quasi-equilibrated across the accessible O-sites at each T-site, $\Delta G_{\mathrm{ads,C_3}}$ were plotted to show the most favorable binding location (O-site) and form (H-bonded alkene or surface-bound alkyl) for each T-site (Figure 5c). Our calculations indicate that propene should adsorb as H-bonded propene at 11 out of 12 T-sites in MFI and bind as 2-propyl−Z at T5 in the MFI intersection. We also observe that propene binds most favorably in the intersection at 9 T-sites, in the sinusoidal channel at T4 and T7, and in the straight channel at T3. This result is partly because most of the 23 accessible O-sites are in the intersection (15) compared to the sinusoidal (5) and straight (3) channels, but there is a slight preference for C_3 adsorption in intersections as seen in Figure 5a. Overall, C_3 adsorption energies vary by 19 kJ $\mathrm{mol^{-1}}$ comparing the strongest-binding site (T12) and weakest binding site (T8), both of which bind propene in intersections.

To gain insights into the factors impacting propene adsorption energies, we constructed a thermochemical cycle that decomposes the adsorption energy into 5 steps:

$$\Delta E_{\mathrm{ads}} = \mathrm{DPE} + \Delta E_{\mathrm{distort}} + \mathrm{PA} + \Delta E_{\mathrm{chem}} + \Delta E_{\mathrm{disp}} \qquad (11)$$

DPE is the deprotonation energy of the acid site, $\Delta E_{\mathrm{distort}}$ is the energy to distort the zeolite framework in the presence of the corresponding adsorbate, PA is the proton affinity of propene to form the adsorbate species, ΔE_{chem} is the chemisorption energy of the corresponding protonated species, and ΔE_{disp} is the dispersive component of the adsorption. Among these, PA is a gas-phase reaction that converts propene into cationic 1-propyl and 2-propyl species in the case of adsorptions to form 1-propyl−Z and 2-propyl−Z. H-bonded propene is not protonated, such that its PA is 0. These large differences in PA between alkyl and H-bonded alkenes are offset by large differences in ΔE_{chem}, which reflects a combination of confinement and the strength of the O−H bond formed in the case of H-bonded propene and the O−C bond formed in the case of propyl−Z species. To facilitate comparisons among these three species in how confinement effects influence their adsorption energies, we will combine PA with ΔE_{chem} steps (Scheme 2)

$$\Delta E_{\mathrm{ads}} = \mathrm{DPE} + \Delta E_{\mathrm{distort}} + \Delta E_{\mathrm{PA+chem}} + \Delta E_{\mathrm{disp}} \qquad (12)$$

DPE was calculated at all O-sites in MFI and ranges ∼30 kJ $\mathrm{mol^{-1}}$, consistent with prior predictions for MFI.[61] DPE averages across each void environment are within 6 kJ $\mathrm{mol^{-1}}$ (1649 kJ $\mathrm{mol^{-1}}$ in the intersection, 1651 kJ $\mathrm{mol^{-1}}$ in the sinusoidal channel, and 1655 kJ $\mathrm{mol^{-1}}$ in the straight channel), suggesting acid strength is not a function of confinement.

Scheme 2. Thermochemical Cycle for Adsorption of C_3H_6 Near an Acid Site as H-Bonded Propene or a Surface Bound Alkyl

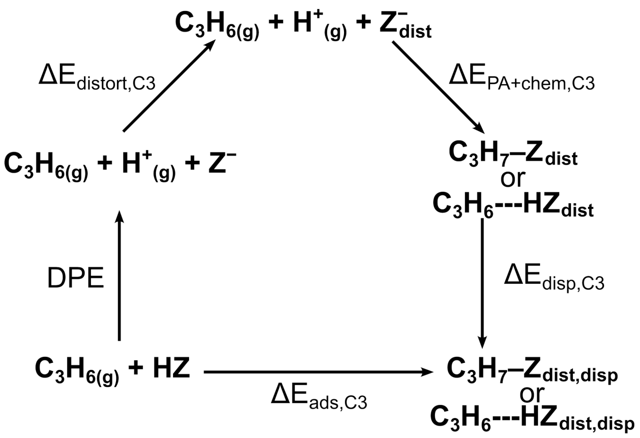

Because changes in DPE are compensated by changes in ΔE_{chem}, as demonstrated in prior work,[62] and do not vary systematically with void environment, these modest changes in DPE are not likely to significantly govern trends in C_3 adsorption. The three remaining energies, $\Delta E_{\mathrm{distort}}$, ΔE_{disp}, and $\Delta E_{\mathrm{PA+chem}}$, are reported for each C_3 adsorbate and averaged across O-sites in each void environment (Figure 6). The distortion energy for a C_3 adsorbate, $\Delta E_{\mathrm{distort,C_3}}$, reflects the energetic penalty to contort the flexible zeolite framework to either mitigate steric constraints or maximize dispersive interactions.[13,42,55] To calculate $\Delta E_{\mathrm{distort,C_3}}$ at each T-site, the adsorbed C_3* species was removed and the energy of the empty distorted anionic framework ($E_{\mathrm{disp,C_3,Z^-_{dist}}}$) was calculated relative to the optimized (nondistorted) structure:

$$\Delta E_{\mathrm{distort,C_3}} = E_{\mathrm{disp,C_3,Z^-_{dist}}} - E_{\mathrm{Z^-}} \qquad (13)$$

The average $\Delta E_{\mathrm{distort,C_3}}$ for each C_3 adsorbate across all the T/O-sites in a given environment is shown in Figure 6b. The average $\Delta E_{\mathrm{distort,C_3}}$ for all C_3 species is lowest in the intersection (88−92 kJ $\mathrm{mol^{-1}}$) compared to the straight (97−107 kJ $\mathrm{mol^{-1}}$) and sinusoidal channels (99−103 kJ $\mathrm{mol^{-1}}$), indicating that channels distort more upon C_3 adsorption, despite the small size of C_3 adsorbates. It is important clarify that this distortion is likely not caused by the zeolite framework flexing to "fit" these small species in the channels, but rather local distortion of the acid site related to the nature of the interaction between the adsorbate and O-site, as discussed further in Section 3.4. Among binding modes, H-bonded propene has the lowest $\Delta E_{\mathrm{distort,C_3}}$ in all three void environments, as expected, because the O−H bond is not replaced with an O−C bond as done in the propyl forms and H-bonded propene can therefore access more stable confirmations with minimal acid site distortion.

The effect of stabilizing adsorbate−framework interactions was assessed by calculating $\Delta E_{\mathrm{disp,C_3}}$ (kJ $\mathrm{mol^{-1}}$):

$$\Delta E_{\mathrm{disp,C3}} = E_{\mathrm{disp,C_3^*}} - \left(E_{\mathrm{disp,Z^-_{dist,C3}}} + E_{\mathrm{disp,C_3(g)}} + E_{\mathrm{disp,H^+(g)}}\right) \qquad (14)$$

using the dispersive energy component of the total DFT-predicted energy for each state, analogous to previous calculations.[13] Although van der Waals interactions include

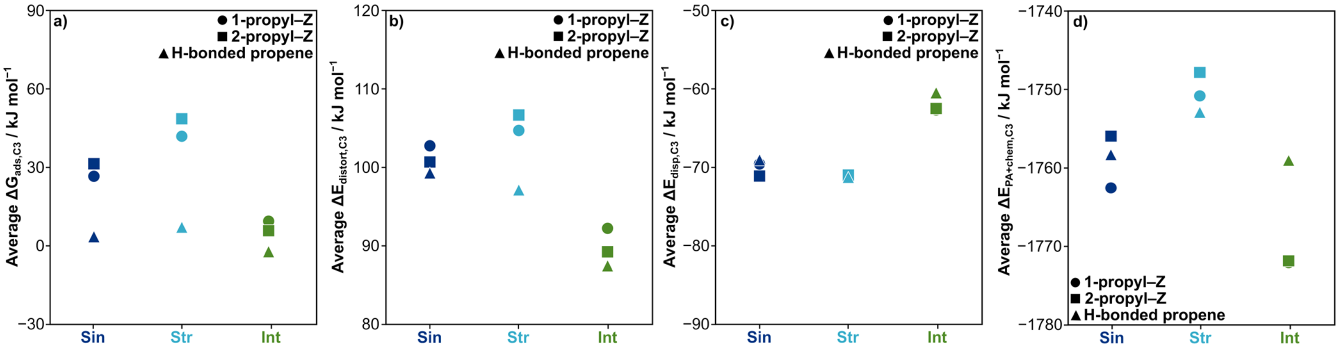

Figure 6. (a) Average $\Delta G_{\text{ads},\text{C}_3}$ (eq 10) at 503 K, (b) average $\Delta E_{\text{distort},\text{C}_3}$ (eq 13) relative to an empty unit cell, (c) average $\Delta E_{\text{disp},\text{C}_3}$ (eq 14), and (d) average $\Delta E_{\text{PA+chem},\text{C}_3}$ (eq 15) for 1-propyl−Z (circles), 2-propyl−Z (squares), and H-bonded propene (triangles) in the sinusoidal channel (dark blue), straight channel (light blue), and intersection (green).

steric repulsion, the dispersive component accounts for only the stabilizing forces and therefore will only become more negative as confinement increases. A more negative $\Delta E_{\text{disp},\text{C}_3}$ corresponds to stronger dispersive interactions and greater stabilization, and C_3 species in the intersection are less stabilized (by ~10 kJ mol^{-1}) on average than species in either channel (Figure 6c). These $\Delta E_{\text{disp},\text{C}_3}$ values decrease within the more-confined MFI channels, despite adsorption energies being lower in intersections than in channels (Figure 6a), because they only describe attractive forces that become more exothermic as void size decreases and do not account for the distortion energies previously discussed. These trends in $\Delta E_{\text{distort},\text{C}_3}$ and $\Delta E_{\text{disp},\text{C}_3}$ indicate that propene species bound in the intersection minimize framework distortions at the expense of weakening dispersive interactions, while binding in the channels strengthens dispersive interactions at the cost of increased distortion. Similar compensations have been reported in prior studies of confinement effects.[6−10] Here, these effects nearly cancel out for H-bonded propene, resulting in approximately constant $\Delta G_{\text{ads},\text{C}_3}$ values across the three environments (Figure 6a), but lead to higher average $\Delta G_{\text{ads},\text{C}_3}$ in the channels for the more sterically restricted 1-propyl−Z and 2-propyl−Z species.

The remaining component of the thermochemical cycle, $\Delta E_{\text{PA+chem},\text{C}_3}$, can be calculated by subtracting $\Delta E_{\text{distort},\text{C}_3}$ and $\Delta E_{\text{disp},\text{C}_3}$ from $\Delta E_{\text{ads},\text{C}_3}$:

$$\Delta E_{\text{PA+chem},\text{C}_3} = \Delta E_{\text{ads},\text{C}_3} - \Delta E_{\text{distort},\text{C}_3} - \Delta E_{\text{disp},\text{C}_3} - \text{DPE} \tag{15}$$

In the case of H-bonded propene, with a PA of 0, $\Delta E_{\text{PA+chem},\text{C}_3}$ solely reflects the chemisorption energy, or the strength of the interaction between the adsorbate and the acid site as well as steric interactions between the adsorbate and the framework. For 1-propyl−Z or 2-propyl−Z, $\Delta E_{\text{PA+chem},\text{C}_3}$ also reflects the protonation and rearrangement of gas phase propene to form these species. Given the different definitions, $\Delta E_{\text{PA+chem},\text{C}_3}$ values between the three species cannot be readily compared. The average $\Delta E_{\text{PA+chem},\text{C}_3}$ across the three void environments varies by only 7 kJ mol^{-1} for H-bonded propene but is more sensitive to environment for 1-propyl−Z and 2-propyl−Z (Figure 6d). This suggests surface-bound alkyls incur greater steric penalties in the smaller channels, which would result in less negative $\Delta E_{\text{PA+chem},\text{C}_3}$ values, likely because the covalent bond constrain these adsorbates closer to the framework compared to H-bonded propene and restricts these species in the confirmations they can adopt. This is further supported by the higher average $\Delta E_{\text{PA+chem},\text{C}_3}$ of 2-propyl−Z, which has fewer degrees of freedom because of the covalent bond to the second carbon atom, compared to 1-propyl−Z in the straight and sinusoidal channels (Figure 6d).

Overall, this thermochemical cycle shows how the flexibility of H-bonded propene results in it being less sensitive to the binding environment than either alkyl form, which are particularly penalized in channel environments. Furthermore, it demonstrates how dispersive interactions are more exothermic in the tighter channel environments than in the less-confined MFI intersections, but that these benefits are—for H-bonded propene—nearly exactly offset by larger distortions of the MFI framework and its resulting energy penalties.

3.3. Hexene-Derived Adsorbates.

C_6 propene dimerization products—hexenes—may serve as a proxy to dimerization transition states and can assess how alkene size and shape (through C_6's distinct skeletal isomers) affect trends in thermodynamic stability. Only the H-bonded form of C_6 alkenes were examined to simplify the configurational space to analyze, given that there are 13 C_6 alkene isomers to consider, and because an H-bonded complex is likely the most stable configuration based on assessment of C_3 adsorbate binding (Figure 5). Formation free energies ($\Delta G_{\text{form},\text{C}_6}$, kJ mol^{-1}) were calculated relative to a bare acid site and two gas phase propene species:

$$\Delta G_{\text{form},\text{C}_6} = G_{\text{C}_6^*} - (G_{\text{H}-\text{Z}} + 2^* G_{\text{C}_3\text{H}_6(\text{g})}) \tag{16}$$

for each of the 13 C_6 H-bonded alkene isomers at all accessible T/O-sites. The reference state of two gas-phase propene molecules was chosen, rather than the corresponding gaseous C_6 alkene, so that each bound C_6 isomer would have the same reference state. Previous experimental work demonstrated double bond isomerization is facile relative to C−C bond formation at propene oligomerization conditions;[54,58−60] therefore, we show here the most favorable double bond isomer for each of the 5 C_6 alkene skeletal isomers at each T-site (Figure 7). Of the 5 skeletal isomers, four were estimated to be equilibrated with one another in MFI, with only 2,2-dimethylbutene present at lower-than-expected concentrations.[54] In agreement with that finding, our calculated $\Delta G_{\text{form},\text{C}_6}$ values are largest for 2,2-dimethylbutene, consistent with its

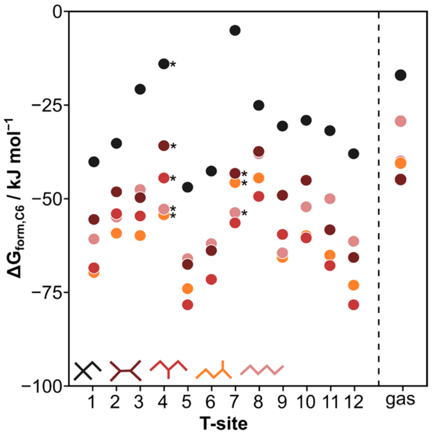

Figure 7. Adsorption free energy ($\Delta G_{form,C_6}$, kJ mol^{-1}, eq 16) at 503 K for the most favorable of each of the 5 skeletal C_6 H-bonded alkene isomers per T-site and in the gas-phase: *n*-hexene (light red), 2-methylpentene (orange), 3-methylpentene (red), 2,3-dimethylbutene (dark red) and 2,2-dimethylbutene (black). All alkenes are at O-sites in the intersection except those with a star, which are in the sinusoidal channel. The corresponding images of the C_6 H-bonded alkene structures are in Figures S34−S45 in the Supporting Information.

inability to form in equilibrium with the other four skeletal isomers, which have much more similar $\Delta G_{form,C_6}$ values and generally trend as 2,3-dimethylbutene > *n*-hexenes >2-methylpentenes >3-methylpentenes. These trends among isomers do not significantly vary with changing Al site. The relative stability of C_6 isomers is generally consistent with the gas phase formation energies, except for 2,3-dimethylbutene, which is the most thermodynamically favored in the gas-phase but is destabilized relative to the other isomers upon confinement. In comparing T-sites, $\Delta G_{form,C_6}$ values vary more for bulkier isomers, such as 2,2-dimethylbutene (a range of 42 kJ mol^{-1}), than for less-bulky isomers, such as *n*-hexenes (a range of 30 kJ mol^{-1}). This, like the variations in adsorption energies observed for C_3, indicates that the zeolite void environment has larger impacts on bulky or sterically hindered adsorbates than those that have greater flexibility. Generally, formation energies of these C_6 species are more sensitive to acid site location than H-bonded propene. Furthermore, C_6 species, like propene, prefer to reside in MFI intersections over MFI channels, with only T4 (the sole T-site without access to the intersection) and some isomers at T7 preferring adsorption at O-sites within the sinusoidal channel as counter-examples.

The same thermochemical cycle proposed for C_3 adsorption (Scheme 2) was applied to C_6 alkene formation (Scheme S1). Similarly to H-bonded propene, there is no protonation of the H-bonded C_6 alkene, but there is rearrangement of the 2 propene molecules to form a C_6, which corresponds to the gas-phase formation energy ($\Delta G_{form,C_6}$, Figure 7). The analogous form of eq 15 was applied to C_6 alkenes to obtain a $\Delta E_{PA+chem,C_6}$, where PA is actually gas-phase $\Delta E_{form,C_6}$, and the gas-phase formation energy of the corresponding isomer was subtracted to obtain $\Delta E_{chem,C_6}$. The values of $\Delta G_{form,C_6}$, $\Delta E_{distort,C_6}$, $\Delta E_{disp,C_6}$ and $\Delta E_{chem,C_6}$ for the best isomer per O-site were averaged across the three void environments for all five C_6 structural isomers (Figure 8). Following the same trend observed for C_3 adsorbates, the strongest binding (lowest $\Delta G_{form,C_6}$), the smallest distortion energies, and the weakest (least negative) dispersive energies are in MFI intersections. Whereas H-bonded propene had comparable average $\Delta G_{ads,C_3}$ values across the three void environments (Figure 6a), the average $\Delta G_{form,C_6}$ of all C_6 isomers increases by 10−56 kJ mol^{-1} in the sinusoidal channel and 20−43 kJ mol^{-1} in the straight channel compared to the intersection (Figure 8a). Just as surface-bound propyl−Z structures appear to exacerbate the effect of confinement on $\Delta G_{ads,C_3}$ compared to H-bonded propene, increasing the pi-bonded alkene size from C_3 to C_6, and increasing its branching, similarly results in consistently higher average $\Delta G_{form,C_6}$ values in the more confined MFI channels.

Comparing $\Delta E_{distort,C_6}$ (Figure 8b), bulkier 2,2-dimethylbutene and 2,3-dimethylbutene have larger distortion energies in MFI channels than *n*-hexenes, 3-methylpentenes, or 2-methylpentenes. Distortion energies are generally lower in intersections, as expected, and show less variation among these skeletal isomers, indicating that MFI intersections are large enough to accommodate all isomers without significant distortions of the framework. As expected from propene adsorption data, the MFI intersection has the weakest dispersive interactions among the three environments and is nearly constant for all five isomers, suggesting they experience similar stabilization in the larger void environment despite

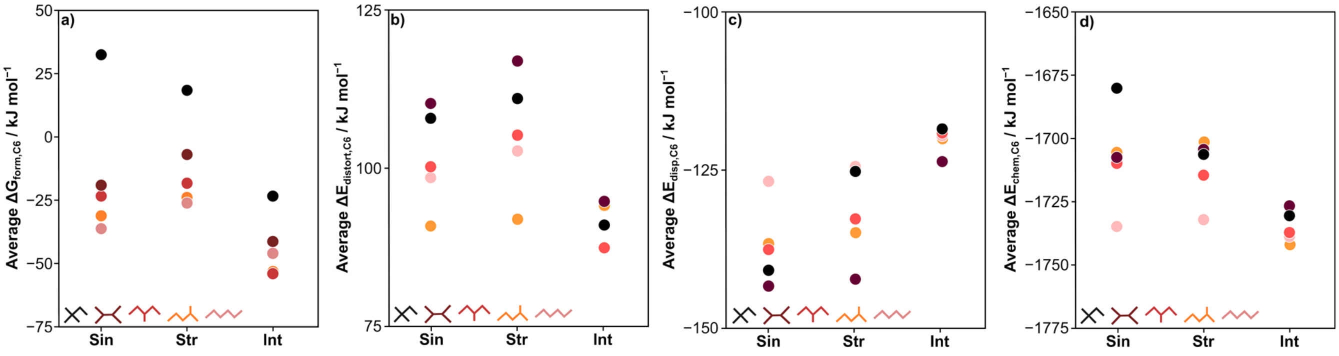

Figure 8. (a) Average $\Delta G_{form,C_6}$ (eq 16) at 503 K, (b) average $\Delta E_{distort,C_6}$ (eq S5) relative to an empty unit cell, (c) average $\Delta E_{disp,C_6}$ (eq S6), and (d) average $\Delta E_{chem,C_6}$ (eq S7) in the sinusoidal channel, straight channel, and intersection for each of the 5 skeletal C_6 H-bonded alkene isomers: *n*-hexene (light red), 2-methylpentene (orange), 3-methylpentene (red), 2,3-dimethylbutene (dark red) and 2,2-dimethylbutene (black).

Scheme 3. Propene Dimerization Between a (a, b) 1° Alkyl and Propene or (c, d) a 2° Alkyl and Propene. Our DFT Calculations Predict the Lowest Δ$G^{‡}$ (eq 9) for the Pathway Highlighted in Blue.

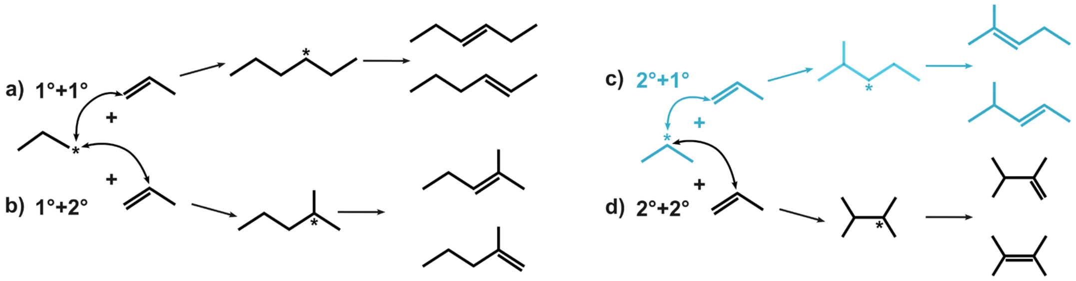

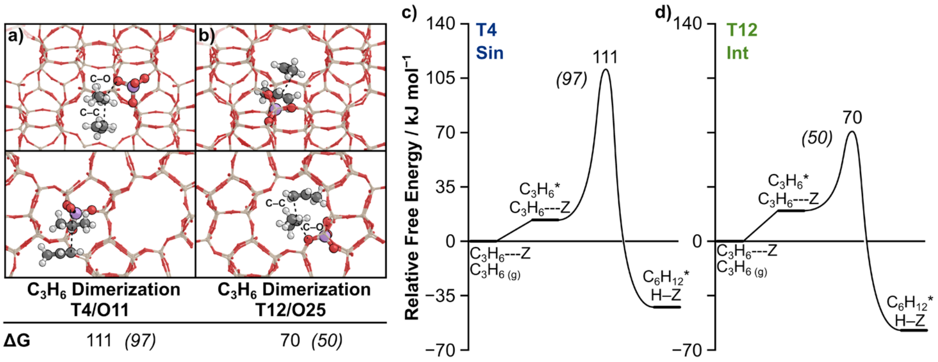

Figure 9. C_3H_6 dimerization transition state structure at (a) T4/O11 and (b) T12/O25 viewed through the sinusoidal (top) and straight (bottom) channels. Reaction coordinate diagram for C_3H_6 dimerization at (c) T4 and (d) T12 with effective and intrinsic (italics) free energy barriers at 503 K.

different degrees of branching. More negative average $\Delta E_{\mathrm{disp,C_6}}$ values are observed in the channels for all species, but the range is isomer dependent, with *n*-hexene being the least stabilized compared to the intersection while 2,3-dimethylbutene is the most stabilized. For C_6 species, given the propene reference states, the $\Delta E_{\mathrm{chem,C_6}}$ values reflect less negative chemisorption in the channels for all isomers, except *n*-hexene with approximately constant values, consistent with greater unfavorable steric interactions between the framework and adsorbate that are exacerbated by increased branching. These results demonstrate that H-bonded C_6 alkenes are destabilized in the smaller channel environments relative to the intersection with bulkier isomers such as 2,2-dimethylbutene and 2,3-dimethylbutene penalized to an even greater extent.

3.4. Propene Dimerization. Next, we studied the influence of void environment on propene dimerization barriers. Propene dimerization has been proposed to occur through one of two routes. In the "sequential" route, a H-bonded propene is protonated to form a surface-bound alkyl, followed by the alkyl detaching from the framework to form a carbocation that interacts with the C=C bond of a vicinal propene to form a $C_6H_{13}^{+}$ carbocation, which can then deprotonate to form a C_6 alkene.[53,63,64] In the 'concerted' route, an H-bonded propene is protonated to form a C_3 carbocation that reacts with a vicinal propene to form the same C_6 carbocation.[63,64] These transition states, in our view, generally have no "memory" of whether they proceeded through a bound-alkyl intermediate or not, such that the discussion of whether the mechanism occurs by a sequential or concerted route is likely irrelevant. As soon as the alkyl leaves the surface (in the sequential route) or the H-bonded alkene is protonated (in the concerted route), a C_3 carbocation is formed that, from that point forward, interacts with a propene to dimerize.[63,64] The C_3 carbocation can either be primary or secondary, depending on which C atom is protonated, and that carbocation can interact with either the primary or secondary C atom in the C=C double bond. This results in four possible transition states (Scheme 3) that vary in the substitution of the C_3 and the C_6 carbocations involved and produce distinct skeletal isomers. However, as mentioned, these four skeletal isomers can likely undergo isomerization reactions to form an equilibrated mixture such that the selectivities among these isomers should not necessarily reflect kinetic preferences among their formation pathways.

The first-order effective free energy barrier (Δ$G^{‡}$, kJ mol^{-1}, eq 9) was calculated for all 4 possible dimerization transition state structures at two representative T-sites: T4, with O-sites exclusively in the sinusoidal channel, and T12, with O-sites in the intersection (Figure S48). Because the transition state is agnostic to whether the mechanism is sequential or concerted, we chose the most stable C_3 adsorbate as the reference state. This state is H-bonded propene at all T-sites except T5, where 2-propyl−Z is the most stable C_3 adsorbate. At each T/O-site considered, the transition state between a 2° carbocation and the 1 °C of C_3H_6 had the lowest $\Delta G_1^{‡}$ (Figure S48); therefore, the remainder of our study investigates this transition state structure. This transition state forms 2-methylhexenes, therefore $\Delta G_{\mathrm{form,C_6}}$ for those isomers may be most indicative of transition state stabilities.

We first compared T4 and T12, selected because both T-sites have O-sites in a single void environment (the sinusoidal channels and the intersection, respectively). The most stable propene dimerization transition state for T4 occurs at O11 and, although O11 resides in the sinusoidal channel, the transition state complex is preferentially located at the edge of

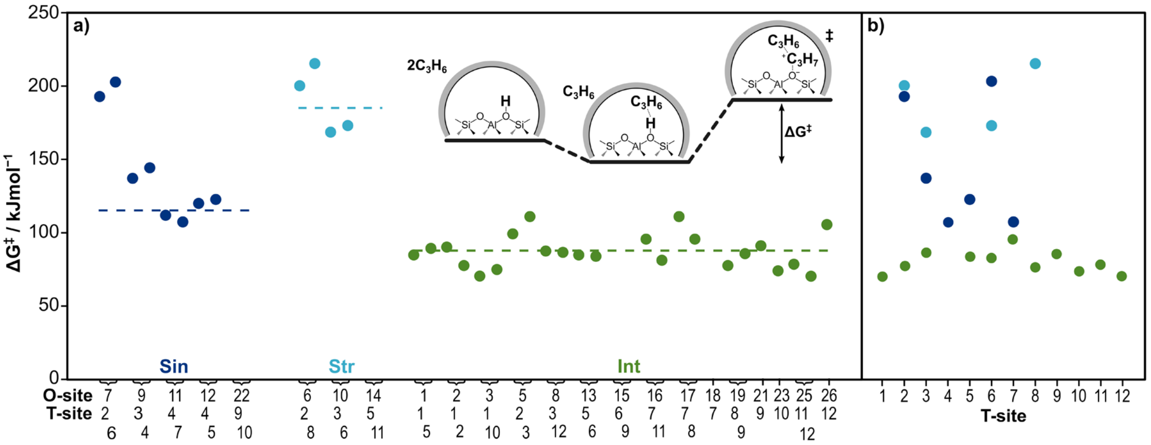

Figure 10. (a) Effective first-order free energy barriers ($\Delta G^{\ddagger}$, kJ mol^{-1}, eq 9) relative to the most stable C_3 adsorbate and gas phase propene in the sinusoidal channel (dark blue), straight channel (light blue), and intersection (green) at 503 K. Average $\Delta G^{\ddagger}$ in each environment is denoted with dashed lines. (b) The lowest $\Delta G^{\ddagger}$ per void environment per T-site. Structures of the best transition state per T-site are shown in Figures S49−S52 in the Supporting Information.

the sinusoidal channel and the intersection (Figure 9a). This suggests that even at T4—the only T-site nominally without access to the intersection—adsorbates may be able to access the boundary of the intersection, albeit with an energetic penalty, depending on their size and the nature of their interactions with the acid site, which may be a pertinent distinction between T4 of MFI and T-sites of TON. At T12, the most favorable transition state resides in the intersection and is associated with O25 (Figure 9b). Propene dimerization has a $\Delta G^{\ddagger}$ of 111 kJ mol^{-1} (Figure 9c) at T4/O11 and 70 kJ mol^{-1} (Figure 9d) at T12/O25. This 41 kJ mol^{-1} difference in $\Delta G^{\ddagger}$ may be partly attributed to framework distortion at T4/O11 to allow the transition state to access the intersection and suggests propene dimerization transition states may prefer to form in the intersection instead of the more restrictive sinusoidal channel. We next expand our analysis of propene dimerization effective barriers to all accessible O-sites in MFI (35 sites out of 48 total O-sites) to more completely capture the effect of void environment on the dimerization transition state.

O-sites in the intersection have consistently lower $\Delta G^{\ddagger}$ values (70−111 kJ mol^{-1}) compared to the sinusoidal channel (106−202 kJ mol^{-1}) and the straight channel (168−214 kJ mol^{-1}) (Figure 10a). The average $\Delta G^{\ddagger}$ value across all 15 intersection O-sites (87 kJ mol^{-1}) is 29 kJ mol^{-1} and 102 kJ mol^{-1} lower than those for the sinusoidal and straight channels, respectively (Figure 10a). The intersection, similarly, had the lowest average $\Delta G_{\mathrm{ads},C_3}$ for H-bonded propene and the lowest $\Delta G_{\mathrm{form},C_6}$ for 2-methylhexenes (and all other isomers); however, the differences among $\Delta G^{\ddagger}$ values are significantly exacerbated between the void environments compared to $\Delta G_{\mathrm{ads},C_3}$ or $\Delta G_{\mathrm{form},C_6}$, suggesting confinement effects are substantially more pronounced for the C_6 transition states than for the C_6 products or the smaller C_3 adsorbates. This could suggest that the C_6 dimerization transition state is larger than the C_6 product, given that the C−C bond is not yet formed in the transition state (which also has one additional H than the product). Despite both void environments comprising 10-MRs, $\Delta G^{\ddagger}$ values for reactions at O-sites in the sinusoidal channel are significantly lower than those in the straight channel. This is somewhat misleading, as many of the dimerization transition states interacting with sinusoidal O sites are able to reach the MFI intersection, such that the transition state exists at the interface between the sinusoidal channel and intersection (e.g., Figure 9a), leading to lower $\Delta G^{\ddagger}$ values.

Given that there are multiple accessible O-sites for a given T-site, and we consider all transition states for those O-sites to be accessible at rates proportional to their free energies, we focus on the transition state with the lowest $\Delta G^{\ddagger}$ per T-site (Figure 10b). In contrast to $\Delta G_{\mathrm{ads},C_3}$ for C_3 species, which sampled all 3 void environments, the most favorable transition states for dimerization are in the MFI intersection for all T-sites except T4, the only T-site without access to the intersection. The most favorable dimerization transition state with at T4 is at the interface between the sinusoidal channel and the MFI intersection, as shown in Figure 9a, and this has the highest $\Delta G^{\ddagger}$ among all T-sites (111 kJ mol^{-1}), 16 kJ mol^{-1} greater than the next highest $\Delta G^{\ddagger}$ at T7 (95 kJ mol^{-1}, Figure 10b) and 41 kJ mol^{-1} higher than the lowest $\Delta G^{\ddagger}$ at T1. Similar trends in $\Delta G^{\ddagger}$ with void environment were also observed when calculated relative to a bare site instead of H-bonded propene (i.e., the second-order barrier, Figure S53). Previous DFT calculations predict that TPA^+ will preferentially site Al to T12 while DABCO biases Al to T4.[25,26] As such, these transition state energies would predict lower propene dimerization rates on samples synthesized with DABCO or EDA as the Al distribution is shifted from T12, with a $\Delta G^{\ddagger}$ of 70 kJ mol^{-1}, to T4, with a $\Delta G^{\ddagger}$ of 111 kJ mol^{-1} (Figure 10b). More generally, our prior work on toluene methylation strongly suggests that DABCO and EDA bias protons toward confined channels.[25] Here, our data suggests, again, that those channels would result in higher activation energies and lower rates for propene dimerization. However, this is the opposite of the trend we observe for experimentally measured dimerization rates: TON > MFI-DABCO/MFI-EDA > MFI-TPA (Figure 3 and Table 2). To further understand the trends in the DFT data, we again utilize a thermochemical cycle for $\Delta G^{\ddagger}$, as we did earlier for propene and hexene adsorption energies, to describe these $\Delta G^{\ddagger}$ values in terms of distortion, dispersion, and chemisorptive (and electrostatic) interaction energies.

The $\Delta G^{\ddagger}$ is relative to a C_3 adsorbate, therefore, the relevant distortion, dispersion, and chemisorptive energies are also

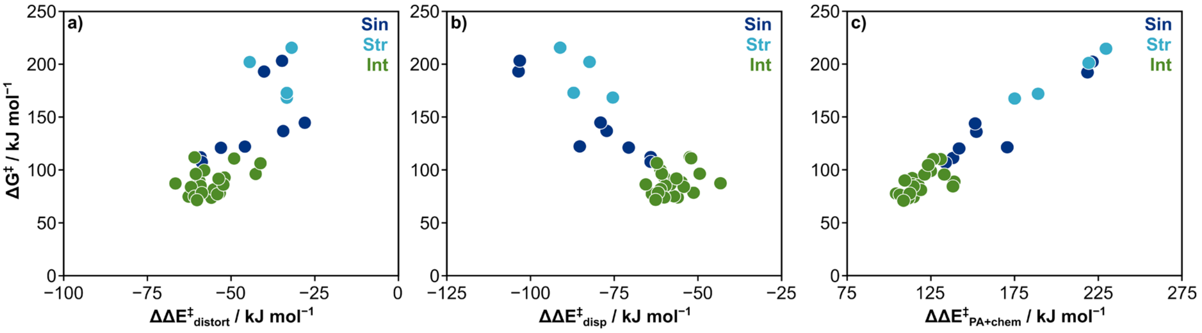

Figure 11. $\Delta G^{\ddagger}$ barriers versus (a) $\Delta\Delta E^{\ddagger}_{\text{distort}}$ (eq 17), (b) $\Delta\Delta E^{\ddagger}_{\text{disp}}$ (eq 18) and (c) $\Delta\Delta E^{\ddagger}_{\text{PA+chem}}$ (eq 19) in the sinusoidal channel (dark blue), straight channel (light blue) and intersection (green) at 503 K.

relative to a C_3 adsorbate (see Scheme S2, Supporting Information for more details). For example, the relevant distortion energy for $\Delta G^{\ddagger}$ is the difference between the distortions required to accommodate the dimerization transition state ($\Delta E^{\ddagger}_{2,\text{distort}}$) relative to a protonated surface and that to accommodate H-bonded propene ($\Delta E_{\text{distort},C_3}$):

$$\Delta\Delta E^{\ddagger}_{\text{distort}} = \Delta E^{\ddagger}_{2,\text{distort}} - \Delta E_{\text{distort},C_3} \quad (17)$$

with similar $\Delta\Delta E^{\ddagger}$ values that can be constructed for dispersive interactions and chemisorptive/electrostatic interactions (lumped, as before, with gas-phase proton affinities).

The differences in distortion energies between the dimerization transition state and bound propene, $\Delta\Delta E^{\ddagger}_{\text{distort}}$, are negative, counterintuitively, because the C_6 transition state complexes require less framework distortion than the C_3 adsorbates despite their larger size. This arises because of the different nature of interactions between the two adsorbates and the confining framework. C_3H_6 interacts with a proton through H-bonding, while the cationic transition state interacts electrostatically with an anionic framework oxygen formed upon lattice deprotonation. The cationic transition state can thus move further away from lattice atoms, allowing it to reside in the middle of the pore to alleviate steric penalties with minimal local distortion of the Al−O−Si bonds comprising the active site (Figure S54). $\Delta\Delta E^{\ddagger}_{\text{distort}}$ values are more negative for transition states in the intersection than those in the straight or sinusoidal channels, as expected, because the transition states distort the framework less when located in the larger MFI intersections. $\Delta G^{\ddagger}$ values generally decrease as $\Delta E^{\ddagger}_{\text{distort}}$ becomes more negative (Figure 11a), again consistent with our expectations, as $\Delta G^{\ddagger}$ values will be lower for transition states (in MFI intersections) that cause less distortion of the anionic framework. These result are consistent with trends observed for C_3 and C_6 adsorption energies, suggesting minimal framework distortion in the intersection corresponds to more favorable average $\Delta G_{\text{ads},C_3}$ and $\Delta G_{\text{form},C_6}$ values compared to the more confined straight and sinusoidal channels.

We also calculated the difference in dispersive interaction energies, $\Delta\Delta E^{\ddagger}_{\text{disp}}$:

$$\Delta\Delta E^{\ddagger}_{\text{disp}} = \Delta E^{\ddagger}_{2,\text{disp}} - \Delta E_{\text{disp},C_3} \quad (18)$$

and these values can be compared to E_{VDW} reported in previous work.[13] $\Delta\Delta E^{\ddagger}_{\text{disp}}$ values are negative at all O-sites, indicating the transition state has more dispersive interactions than the C_3 precursor, as expected given its larger size. In the previous work, reported E_{VDW} values (approximately −115 kJ mol^{-1} for TON, −50 kJ mol^{-1} for MFI, and −15 kJ mol^{-1} for FAU) became less negative with increasing void size because of weaker adsorbate−framework interactions, and the value for MFI reflected its intersections.[13] Our $\Delta\Delta E^{\ddagger}_{\text{disp}}$ values (Figure 9b) range from −103 to −43 kJ mol^{-1} across the 12 T-sites in MFI (Figure 11b) with values in the MFI intersections (avg: −57 kJ mol^{-1}) being close to that reported in previous work (−50 kJ mol^{-1}), and our values in MFI channels (avg: −82 kJ mol^{-1}) closer to that reported for TON in previous work (−115 kJ mol^{-1}). This wide range in $\Delta\Delta E^{\ddagger}_{\text{disp}}$ in MFI further indicates the heterogeneity in low-symmetry frameworks that becomes apparent when all T/O-sites are considered. Counterintuitively, $\Delta G^{\ddagger}$ values increase as $\Delta\Delta E^{\ddagger}_{\text{disp}}$ values become more negative, suggesting that greater dispersive stabilization does not lower barriers. This negative correlation was also observed for C_3 and C_6 adsorption energies, and simply reflects that dispersive contributions are only attractive and do not include the repulsive interactions (e.g., steric constraints) that are also present in van der Waals forces. This is because those repulsive interactions are captured by DFT without the need for additional terms (i.e., without the need for DFT-D*x* methods) and thus are within the chemisorptive terms of our thermochemical cycle, along with electrostatic interactions. The trade-off between stabilizing dispersive interactions and destabilizing repulsive interactions as the adsorbate size approaches that of the void has been thoroughly studied,[6−10] and our results indicate that propene dimerization transition states in the sinusoidal and straight channels of MFI are in the regime in which the steric penalties outweigh the benefit of enhanced dispersive interactions.

Lastly, $\Delta\Delta E^{\ddagger}_{\text{PA+chem}}$ is calculated by adding $\Delta E^{\ddagger}_{2\text{PA+chem}}$ and $-\Delta E_{\text{PA+chem},C_3}$:

$$\Delta\Delta E^{\ddagger}_{\text{PA+chem}} = \Delta E^{\ddagger}_{2,\text{PA+chem}} - \Delta E_{\text{chem},C_3} \quad (19)$$

Its values are positive at all T/O-sites (Figure 11c) because the electrostatic interactions between the cationic transition state and the anionic framework are weaker than the covalent and H-bonding interactions associated with the formation of the O−H bond present in the H-bonded propene reference state. Although DPE, strictly speaking, cancels out in the thermochemical cycle used to represent the first-order barriers (Scheme S2), acid strength still influences the barrier because DPE strongly correlates to the strength of the electrostatic interactions between cationic transition states and anionic conjugate bases, as described in prior work.[62,65] Comparing different MFI environments, $\Delta\Delta E^{\ddagger}_{\text{1PA+chem}}$ values are generally lower in the intersection (105−139 kJ mol^{-1}) compared to the sinusoidal (134−222 kJ mol^{-1}) and straight (175−230 kJ mol^{-1}) channels. Higher $\Delta E^{\ddagger}_{\mathrm{PA+chem}}$ values in the channels, and their correlation with higher $\Delta G^{\ddagger}_{\mathrm{I}}$ values, is likely indicative of greater steric repulsions experienced by the transition states in the tighter channels compared to the intersection.

Overall, the trends among $\Delta G^{\ddagger}$ values resemble those observed for hexene adsorption energies, with distortion and steric constraints showing that tighter confinement within MFI channels results in higher barriers and less-favorable adsorption, respectively. In contrast, dispersive interactions, when taken alone, give misleading results and negatively correlate with barriers and adsorption energies. As stated above, these computational predictions suggest that kinetically determined rates should be lower in TON than in MFI, and lower in EDA- or DABCO-based MFI samples than in TPA-based MFI samples, in contradiction to experimentally measured data. However, measured data (Figure 3) reflect convolutions of kinetic and transport effects, and the slopes in Figure 3 represent $\sqrt{k_{\mathrm{eff}}D_{\mathrm{e}}}$ values in the limit of severe mass transport limitations. Evidence for such intrazeolite mass transport limitations have been shown in our previous work;[23] for example, propene dimerization rates on TON increased with increasing inverse crystallite size (per H$^+$, 503 K, 16−607 kPa C_3H_6, 0.19−1.1 μm^{-1}). Thus, given that DFT suggests that k_{eff} decreases with void size, then D_{e} must increase with decreasing void size by larger amounts than k_{eff} decreases to rationalize the increase in $\sqrt{k_{\mathrm{eff}}D_{\mathrm{e}}}$ values with decreasing void size as shown in Figure 3. Again, this is a counterintuitive result considering only the transport barriers imposed by the inorganic framework and pore structure, which would suggest that effective diffusivities would be lower (or at least similar) in TON than in MFI, given that diffusion in either framework requires transport through 10-MR pores.

These apparent inconsistencies are resolved, as discussed in greater detail in our prior work,[23,28,66] by recognizing that the effective diffusivity of propene depends strongly on the presence of intrapore heavier alkene products, formed during oligomerization catalysis, that slowly diffuse out of the zeolite. These intrapore product alkenes lead to apparent deactivation behavior as reaction rates decrease with time-on-stream, which actually reflects an approach toward steady-state behavior as their intrapore concentrations increase (thus, decreasing D_{e}). Transients in propene dimerization rates persistent over many turnovers upon step changes in reaction temperature or propene pressure demonstrate that the extent of diffusional constraints depends on the composition of the intrapore alkene phase (Figure S55, Supporting Information).[23,24] Therefore, zeolite materials (or reaction conditions) that favor dimerization over the formation of heavier products ($C_{\geq 9}$) should lead to higher D_{e} values, which might offset decreases in k_{eff} and result in the larger $\sqrt{k_{\mathrm{eff}}D_{\mathrm{e}}}$ observed in Figure 3. Indeed, TON has a higher measured selectivity to dimers over $C_{\geq 9}$ products and higher $\sqrt{k_{\mathrm{eff}}D_{\mathrm{e}}}$ values (Figure 3) compared to TPA-based MFI.[23] Differences in product distribution at iso-conversion are also observed for EDA- or DABCO-based MFI samples compared to TPA-based MFI, which would indicate changes to the composition of intrapore occluded hydrocarbons and, in turn, D_{e} values (discussed in more detail in Section S20, Supporting Information). Altogether, this suggests that transport and selectivity effects, which are intertwined, dominate the differences in observed rates (and $\sqrt{k_{\mathrm{eff}}D_{\mathrm{e}}}$) among TON and MFI samples synthesized with different SDAs, and at different propene pressures (Table 2).

4. CONCLUSIONS

Propene dimerization turnover rates (per H$^+$, 315 kPa C_3H_6, 503 K) were ∼9× lower on MFI-TPA, with Al sites biased to the intersections, than on MFI-DABCO and MFI-EDA, with Al sites biased to the channels. Because of the convolution of kinetic and transport processes within zeolite pores, higher measured rates on MFI-DABCO and MFI-EDA samples compared to MFI-TPA may reflect an increase in the intrinsic dimerization rate constants, the alleviation of diffusion limitations, or both. Therefore, DFT was used to isolate and assess the influence of void size on propene dimerization kinetics.

DFT-predicted adsorption energies indicate that H-bonded propene is the most favorable C_3 adsorbate in all void environments, and that surface-bound 1-propyl−Z and 2-propyl−Z are destabilized relative to H-bonded propene to a greater extent in the channels compared to the intersection. Although the effect of void environment on H-bonded propene is minimal, average $\Delta G_{\mathrm{form},C_6}$ values for all C_6 H-bonded alkene isomers are 10−56 kJ mol^{-1} lower in the intersection compared to the channels, with highly branched C_6 isomers destabilized to a greater extent in the channels relative to more linear C_6 isomers. Propene dimerization transition states are also destabilized relative to C_3 precursors in the channels, and the most favorable transition state per T-site is in the intersection at all T-sites except T4, the only T-site without direct access to the intersection. Trends in the stability of C_3 adsorbates, C_6 H-bonded alkenes, and dimerization transition states with void environment were further analyzed by using thermochemical cycles to isolate the contributions of framework distortion ($\Delta E_{\mathrm{distort}}$), dispersive interactions (ΔE_{disp}), and the gas-phase rearrangement and chemisorption ($\Delta E_{\mathrm{PA+chem}}$). Although dispersive energies for the transition state structures were more negative in the channels, corresponding to stronger dispersive stabilizations, the effective free energy barriers were higher. Combined with a decrease in effective free energy barriers with decreasing distortion energies, this suggests that increased steric hindrance and framework distortion plays a larger role than enhanced dispersive interactions on the adsorbate stability with increasing confinement.

These DFT data suggest that the higher turnover rates in DABCO- and EDA-synthesized MFI compared to TPA-based MFI occur despite decreases in intrinsic rates, suggesting a strong alleviation of mass transport effects through increasing the effective diffusivity of propene. This also suggests that higher turnover rates in TON compared to all MFI samples are similarly caused by alleviations of mass transport limitations through higher propene diffusivities rather than by increases in intrinsic dimerization rates. These increases in effective diffusivities in DABCO- and EDA-synthesized MFI are likely caused by changes in product selectivity to species with different carbon number or branching, as preliminarily evinced by shifts in the product distribution at iso-conversion among TON, MFI-EDA/DABCO, and MFI-TPA. More generally, this study uses DFT to isolate the effect of Al location on intrinsic kinetics in heterogeneous MFI zeolites. This approach illustrates how to quantitatively describe trade-offs between stabilizing dispersive interactions and destabilizing steric penalties with increasing confinement for propene dimerization transition states and reactive intermediates, revealing that steric interactions and framework distortion can exert stronger influences on the stability of smaller adsorbates that are charge-neutral and thus reside more closely to the lattice than larger cationic species.

ASSOCIATED CONTENT

Supporting Information

The Supporting Information is available free of charge at https://pubs.acs.org/doi/10.1021/acscatal.5c00392.

> Zeolite characterization data (XRD, N_2 adsorption isotherms, NH_3 temperature-programmed desorption, ^{27}Al MAS NMR, SEM), supplemental propene oligomerization kinetics and discussion, images of C_3, C_6, and dimerization transition state structures, DFT-predicted DPE values, second order dimerization barriers, thermochemical cycles (PDF)

AUTHOR INFORMATION

Corresponding Authors

Rajamani Gounder − *Charles D. Davidson School of Chemical Engineering, Purdue University, West Lafayette, Indiana 47907, United States;* orcid.org/0000-0003-1347-534X; Email: rgounder@purdue.edu

David D. Hibbitts − *Charles D. Davidson School of Chemical Engineering, Purdue University, West Lafayette, Indiana 47907, United States; Department of Chemical Engineering, University of Florida, Gainesville, Florida 32611, United States;* orcid.org/0000-0001-8606-7000; Email: hibbitts@purdue.edu

Authors

Lauren Kilburn − *Charles D. Davidson School of Chemical Engineering, Purdue University, West Lafayette, Indiana 47907, United States; Department of Chemical Engineering, University of Florida, Gainesville, Florida 32611, United States*

Diamarys Salomé Rivera − *Charles D. Davidson School of Chemical Engineering, Purdue University, West Lafayette, Indiana 47907, United States*

Elizabeth E. Bickel Rogers − *Charles D. Davidson School of Chemical Engineering, Purdue University, West Lafayette, Indiana 47907, United States*

Complete contact information is available at: https://pubs.acs.org/10.1021/acscatal.5c00392

Notes

The authors declare no competing financial interest.

ACKNOWLEDGMENTS

The authors (L.K., D.S.R., E.B.R., R.G.) acknowledge financial support provided by the National Science Foundation under Cooperative Agreement no. EEC-1647722, which is an Engineering Research Center for the Innovative and Strategic Transformation of Alkane Resources. L.K. acknowledges financial support from the UF Department of Chemical Engineering Excellence in Research scholarship. D.H. acknowledges financial support provided by the NSF CAREER program under award CBET-1942684. L.K. and D.H. acknowledge computational resources from the Extreme Science and Engineering Discovery Environment (XSEDE) and the Advanced Cyberinfrastructure Coordination Ecosystem: Services & Support (ACCESS), supported by NSF grant no. ACI-1548562 through allocation CTS160041, and the University of Florida Research Computing.

REFERENCES

(1) Corma, A. Inorganic Solid Acids and Their Use in Acid-Catalyzed Hydrocarbon Reactions. *Chem. Rev.* **1995**, *95* (3), 559−614.

(2) Lercher, J. A.; Seshan, K. Sorption and Activation of Hydrocarbons by Molecular Sieves. *Curr. Opin. Solid State Mater. Sci.* **1997**, *2* (1), 57−62.

(3) Tanabe, K.; Hölderich, W. F. Industrial Application of Solid Acid−Base Catalysts. *Appl. Catal. Gen.* **1999**, *181* (2), 399−434.

(4) Baerlocher, C.; McCusker, L. B. Database of Zeolite Structures. https://america.iza-structure.org/IZA-SC/ftc_table.php (accessed Aug 1, 2022).

(5) First, E. L.; Gounaris, C. E.; Wei, J.; Floudas, C. A. Computational Characterization of Zeolite Porous Networks: An Automated Approach. *Phys. Chem. Chem. Phys.* **2011**, *13* (38), 17339.

(6) Chai, Y.; Dai, W.; Wu, G.; Guan, N.; Li, L. Confinement in a Zeolite and Zeolite Catalysis. *Acc. Chem. Res.* **2021**, *54* (13), 2894−2904.

(7) Gounder, R.; Iglesia, E. The Catalytic Diversity of Zeolites: Confinement and Solvation Effects within Voids of Molecular Dimensions. *Chem. Commun.* **2013**, *49* (34), 3491.

(8) Jones, A. J.; Zones, S. I.; Iglesia, E. Implications of Transition State Confinement within Small Voids for Acid Catalysis. *J. Phys. Chem. C* **2014**, *118* (31), 17787−17800.

(9) Grifoni, E.; Piccini, G.; Lercher, J. A.; Glezakou, V.-A.; Rousseau, R.; Parrinello, M. Confinement Effects and Acid Strength in Zeolites. *Nat. Commun.* **2021**, *12* (1), 2630.

(10) Bhan, A.; Iglesia, E. A. Link between Reactivity and Local Structure in Acid Catalysis on Zeolites. *Acc. Chem. Res.* **2008**, *41* (4), 559−567.

(11) Ferri, P.; Li, C.; Millán, R.; Martínez-Triguero, J.; Moliner, M.; Boronat, M.; Corma, A. Impact of Zeolite Framework Composition and Flexibility on Methanol-To-Olefins Selectivity: Confinement or Diffusion? *Angew. Chem.* **2020**, *132* (44), 19876−19883.

(12) Ferri, P.; Li, C.; Paris, C.; Rodríguez-Fernández, A.; Moliner, M.; Boronat, M.; Corma, A. The Limits of the Confinement Effect Associated to Cage Topology on the Control of the MTO Selectivity. *ChemCatChem* **2021**, *13* (6), 1578−1586.

(13) Sarazen, M. L.; Doskocil, E.; Iglesia, E. Catalysis on Solid Acids: Mechanism and Catalyst Descriptors in Oligomerization Reactions of Light Alkenes. *J. Catal.* **2016**, *344*, 553−569.

(14) Wang, S.; Iglesia, E. Catalytic Diversity Conferred by Confinement of Protons within Porous Aluminosilicates in Prins Condensation Reactions. *J. Catal.* **2017**, *352*, 415−435.

(15) Olsbye, U.; Svelle, S.; Bjørgen, M.; Beato, P.; Janssens, T. V. W.; Joensen, F.; Bordiga, S.; Lillerud, K. P. Conversion of Methanol to Hydrocarbons: How Zeolite Cavity and Pore Size Controls Product Selectivity. *Angew. Chem., Int. Ed.* **2012**, *51* (24), 5810−5831.

(16) Janda, A.; Vlaisavljevich, B.; Lin, L.-C.; Smit, B.; Bell, A. T. Effects of Zeolite Structural Confinement on Adsorption Thermodynamics and Reaction Kinetics for Monomolecular Cracking and Dehydrogenation of N-Butane. *J. Am. Chem. Soc.* **2016**, *138* (14), 4739−4756.

(17) Van der Mynsbrugge, J.; De Ridder, J.; Hemelsoet, K.; Waroquier, M.; Van Speybroeck, V. Enthalpy and Entropy Barriers Explain the Effects of Topology on the Kinetics of Zeolite-Catalyzed Reactions. *Chem. − Eur. J.* **2013**, *19* (35), 11568−11576.

(18) Bhan, A.; Allian, A. D.; Sunley, G. J.; Law, D. J.; Iglesia, E. Specificity of Sites within Eight-Membered Ring Zeolite Channels for Carbonylation of Methyls to Acetyls. *J. Am. Chem. Soc.* **2007**, *129* (16), 4919−4924.

(19) Gounder, R.; Iglesia, E. Effects of Partial Confinement on the Specificity of Monomolecular Alkane Reactions for Acid Sites in Side Pockets of Mordenite. *Angew. Chem., Int. Ed.* **2010**, *49* (4), 808−811.

(20) Muraza, O. Maximizing Diesel Production through Oligomerization: A Landmark Opportunity for Zeolite Research. *Ind. Eng. Chem. Res.* **2015**, *54* (3), 781−789.

(21) Nicholas, C. P. Applications of Light Olefin Oligomerization to the Production of Fuels and Chemicals. *Appl. Catal. Gen.* **2017**, *543*, 82−97.

(22) Chen, N. Y.; Garwood, W. E. Industrial Application of Shape-Selective Catalysis. *Catal. Rev.* **1986**, *28* (2−3), 185−264.

(23) Bickel, E. E.; McGinness, H.; Zamiechowski, N.; Gounder, R. Synthetic Methods to Vary Crystallite Properties of TON Zeolites and Their Consequences for Brønsted-Acid Catalyzed Propene Oligomerization. *J. Catal.* **2023**, *426*, 189−199.

(24) Bickel, E. E.; Gounder, R. Hydrocarbon Products Occluded within Zeolite Micropores Impose Transport Barriers That Regulate Brønsted Acid-Catalyzed Propene Oligomerization. *JACS Au* **2022**, *2* (11), 2585−2595.

(25) Ezenwa, S.; Montalvo-Castro, H.; Hoffman, A. J.; Locht, H.; Attebery, J.; Jan, D.-Y.; Schmithorst, M.; Chmelka, B.; Hibbitts, D.; Gounder, R. Synthetic Placement of Active Sites in MFI Zeolites for Selective Toluene Methylation to Para-Xylene. *J. Am. Chem. Soc.* **2024**, *146* (15), 10666−10678.

(26) Nimlos, C. T.; Hoffman, A. J.; Hur, Y. G.; Lee, B. J.; Di Iorio, J. R.; Hibbitts, D. D.; Gounder, R. Experimental and Theoretical Assessments of Aluminum Proximity in MFI Zeolites and Its Alteration by Organic and Inorganic Structure-Directing Agents. *Chem. Mater.* **2020**, *32* (21), 9277−9298.

(27) Hur, Y. G.; Kester, P. M.; Nimlos, C. T.; Cho, Y.; Miller, J. T.; Gounder, R. Influence of Tetrapropylammonium and Ethylenediamine Structure-Directing Agents on the Framework Al Distribution in B−Al−MFI Zeolites. *Ind. Eng. Chem. Res.* **2019**, *58* (27), 11849−11860.

(28) Bickel, E. E.; Lee, S.; Gounder, R. Influence of Brønsted Acid-Site Density on Reaction-Diffusion Phenomena That Govern Propene Oligomerization Rate and Selectivity in MFI Zeolites. *ACS Catal.* **2023**, *13* (2), 1257−1269.

(29) Katada, N.; Suzuki, K.; Noda, T.; Sastre, G.; Niwa, M. Correlation between Brønsted Acid Strength and Local Structure in Zeolites. *J. Phys. Chem. C* **2009**, *113* (44), 19208−19217.

(30) Gorte, R. J. Temperature-Programmed Desorption for the Characterization of Oxide Catalysts. *Catal. Today* **1996**, *28* (4), 405−414.

(31) Farneth, W. E.; Gorte, R. J. Methods for Characterizing Zeolite Acidity. *Chem. Rev.* **1995**, *95* (3), 615−635.

(32) Kresse, G.; Furthmüller, J. Efficient Iterative Schemes for Ab Initio Total-Energy Calculations Using a Plane-Wave Basis Set. *Phys. Rev. B* **1996**, *54* (16), 11169−11186.

(33) Kresse, G.; Furthmüller, J. Efficiency of Ab-Initio Total Energy Calculations for Metals and Semiconductors Using a Plane-Wave Basis Set. *Comput. Mater. Sci.* **1996**, *6* (1), 15−50.

(34) Kresse, G.; Hafner, J. Ab Initio Molecular Dynamics for Liquid Metals. *Phys. Rev. B* **1993**, *47* (1), 558−561.

(35) Kresse, G.; Hafner, J. Ab Initio Molecular-Dynamics Simulation of the Liquid-Metal–Amorphous-Semiconductor Transition in Germanium. *Phys. Rev. B* **1994**, *49* (20), 14251−14269.

(36) Kravchenko, P.; Plaisance, C.; Hibbitts, D. A New Computational Interface for Catalysis. *ChemRxiv* **2019**.

(37) Blöchl, P. E. Projector augmented-wave method. *Phys. Rev. B* **1994**, *50*, 17953−17979.

(38) Perdew, J. P.; Burke, K.; Ernzerhof, M. Generalized Gradient Approximation Made Simple. *Phys. Rev. Lett.* **1996**, *77* (18), 3865−3868.

(39) Grimme, S. Semiempirical GGA-type density functional constructed with a long-range dispersion correction. *J. Comput. Chem.* **2006**, *27* (15), 1787−1799.

(40) Grimme, S.; Ehrlich, S.; Goerigk, L. Effect of the Damping Function in Dispersion Corrected Density Functional Theory. *J. Comput. Chem.* **2011**, *32* (7), 1456−1465.

(41) van Koningsveld, H. High-Temperature (350 K) Orthorhombic Framework Structure of Zeolite H-ZSM-5. *Acta Crystallogr. B* **1990**, *46* (6), 731−735.

(42) Hoffman, A.; DeLuca, M.; Hibbitts, D. Restructuring of MFI Framework Zeolite Models and Their Associated Artifacts in Density Functional Theory Calculations. *J. Phys. Chem. C* **2019**, *123* (11), 6572−6585.

(43) Monkhorst, H. J.; Pack, J. D. Special Points for Brillouin-Zone Integrations. *Phys. Rev. B* **1976**, *13* (12), 5188−5192.

(44) Jónsson, H.; Mills, G.; Jacobsen, K. W. Nudged Elastic Band Method for Finding Minimum Energy Paths of Transitions. In *Classical and Quantum Dynamics in Condensed Phase Simulations*; World Scientific, 1998; pp 385−404..

(45) Henkelman, G.; Jónsson, H. A Dimer Method for Finding Saddle Points on High Dimensional Potential Surfaces Using Only First Derivatives. *J. Chem. Phys.* **1999**, *111* (15), 7010−7022.

(46) DeLuca, M.; Kravchenko, P.; Hoffman, A.; Hibbitts, D. Mechanism and Kinetics of Methylating C6−C12 Methylbenzenes with Methanol and Dimethyl Ether in H-MFI Zeolites. *ACS Catal.* **2019**, *9* (7), 6444−6460.

(47) DeLuca, M.; Janes, C.; Hibbitts, D. Contrasting Arene, Alkene, Diene, and Formaldehyde Hydrogenation in H-ZSM-5, H-SSZ-13, and H-SAPO-34 Frameworks during MTO. *ACS Catal.* **2020**, *10* (8), 4593−4607.

(48) Ghorbanpour, A.; Rimer, J. D.; Grabow, L. C. Computational Assessment of the Dominant Factors Governing the Mechanism of Methanol Dehydration over H-ZSM-5 with Heterogeneous Aluminum Distribution. *ACS Catal.* **2016**, *6* (4), 2287−2298.

(49) Martinez-Espin, J. S.; De Wispelaere, K.; Westgård Erichsen, M.; Svelle, S.; Janssens, T. V. W.; Van Speybroeck, V.; Beato, P.; Olsbye, U. Benzene Co-Reaction with Methanol and Dimethyl Ether over Zeolite and Zeotype Catalysts: Evidence of Parallel Reaction Paths to Toluene and Diphenylmethane. *J. Catal.* **2017**, *349*, 136−148.

(50) Jones, A. J.; Carr, R. T.; Zones, S. I.; Iglesia, E. Acid Strength and Solvation in Catalysis by MFI Zeolites and Effects of the Identity, Concentration and Location of Framework Heteroatoms. *J. Catal.* **2014**, *312*, 58−68.

(51) Díaz, M.; Epelde, E.; Valecillos, J.; Izaddoust, S.; Aguayo, A. T.; Bilbao, J. Coke Deactivation and Regeneration of HZSM-5 Zeolite Catalysts in the Oligomerization of 1-Butene. *Appl. Catal. B Environ.* **2021**, *291*, 120076.

(52) Dimon, B.; Cartraud, P.; Magnoux, P.; Guisnet, M. Coking Aging and Regeneration of Zeolites. *Appl. Catal. Gen.* **1993**, *101* (2), 351−369.

(53) Mlinar, A. N.; Zimmerman, P. M.; Celik, F. E.; Head-Gordon, M.; Bell, A. T. Effects of Brønsted-Acid Site Proximity on the Oligomerization of Propene in H-MFI. *J. Catal.* **2012**, *288*, 65−73.

(54) Sarazen, M. L.; Doskocil, E.; Iglesia, E. Effects of Void Environment and Acid Strength on Alkene Oligomerization Selectivity. *ACS Catal.* **2016**, *6* (10), 7059−7070.

(55) Sarazen, M. L.; Iglesia, E. Stability of Bound Species during Alkene Reactions on Solid Acids. *Proc. Natl. Acad. Sci. U.S.A.* **2017**, *114* (20), E3900−E3908.

(56) Ren, Q.; Rybicki, M.; Sauer, J. Interaction of C3−C5 Alkenes with Zeolitic Brønsted Sites: π-Complexes, Alkoxides, and Carbenium Ions in H-FER. *J. Phys. Chem. C* **2020**, *124* (18), 10067−10078.

(57) Plessow, N.; Studt, F. Olefin Methylation and Cracking Reactions in H-SSZ-13 Investigated with Ab Initio and DFT Calculations. *Catal. Sci. Technol.* **2018**, *8* (17), 4420−4429.

(58) Buchanan, J. S. Reactions of Model Compounds over Steamed ZSM-5 at Simulated FCC Reaction Conditions. *Appl. Catal.* **1991**, *74* (1), 83−94.

(59) Buchanan, J. S.; Santiesteban, J. G.; Haag, W. O. Mechanistic Considerations in Acid-Catalyzed Cracking of Olefins. *J. Catal.* **1996**, *158* (1), 279−287.

(60) Abbot, J.; Wojciechowski, B. W. The Mechanism of Catalytic Cracking of N-Alkenes on ZSM-5 Zeolite. *Can. J. Chem. Eng.* **1985**, *63* (3), 462−469.

(61) Jones, A. J.; Iglesia, E. The Strength of Brønsted Acid Sites in Microporous Aluminosilicates. *ACS Catal.* **2015**, *5* (10), 5741−5755.

(62) Carr, R. T.; Neurock, M.; Iglesia, E. Catalytic Consequences of Acid Strength in the Conversion of Methanol to Dimethyl Ether. *J. Catal.* **2011**, *278* (1), 78−93.

(63) Svelle, S.; Kolboe, S.; Swang, O. Theoretical Investigation of the Dimerization of Linear Alkenes Catalyzed by Acidic Zeolites. *J. Phys. Chem. B* **2004**, *108* (9), 2953−2962.

(64) Namuangruk, S.; Pantu, P.; Limtrakul, J. Investigation of Ethylene Dimerization over Faujasite Zeolite by the ONIOM Method. *ChemPhysChem* **2005**, *6* (7), 1333−1339.

(65) Blaszkowski, S. R.; van Santen, R. A. Theoretical Study of the Mechanism of Surface Methoxy and Dimethyl Ether Formation from Methanol Catalyzed by Zeolitic Protons. *J. Phys. Chem. B* **1997**, *101* (13), 2292−2305.

(66) Rogers, E. E. B.; Gounder, R. Assessing the Influences of Kinetics and Intrazeolite Diffusion on Propene Oligomerization Product Selectivity in MFI Zeolites. *J. Catal.* **2024**, *438*, 115721.